Revision 2

Garnet as a major carrier of the Y and REE in the granitic rocks: An example from the layered anorogenic granite in the Brno Batholith, Czech Republic

Sven Hönig[1], Renata Čopjaková[1], Radek Škoda[1], Milan Novák[1], David Dolejš[2], Jaromír Leichmann[1], and Michaela Vašinová Galiová[3,4]

[1]Department of Geological Sciences, Masaryk University, Kotlářská 2, 611 37 Brno, Czech Republic

[2]Institute of Petrology and Structural Geology, Charles University, Albertov 6, 128 43 Praha 2, Czech Republic

[3]Department of Chemistry, Faculty of Science, Masaryk University, Kotlářská 2, 611 37 Brno, Czech Republic

[4]Central European Institute of Technology (CEITEC), Masaryk University, Kamenice 5, 625 00 Brno, Czech Republic

ABSTRACT

Garnet and other rock-forming minerals from A-type granite dykes in the Pre-Variscan Brno Batholith were analysed to determine relative contributions of individual minerals to whole rock Y and REE budget and to assess incorporation mechanisms of these elements in garnet. Minor to accessory garnet (< 2 vol%) is the essential reservoir for Y+REE in the Hlína granite accounting ~84 % Y and 61 % REE of the total whole rock budget. Zircon is another important carrier of

REE with ~13 % Y and ~11 % REE. At least ~21 % REE and 1 % Y were probably hosted by Th- and U-rich monazite that has been completely altered to a mixture of secondary REE-bearing phases. The contribution of major rock-forming minerals (quartz and feldspars) is low (~1 % Y; 10 % LREE; ~1 % HREE) excluding Eu, which is hosted predominantly by feldspars (~90 %). Minor to accessory muscovite and magnetite incorporate ~1 % Y and ~2 % REE of the whole rock budget. Magmatic garnet $Sps_{41–46}Alm_{28–44}And_{0–13}Grs_{6–12}Prp_{0–1}$ is Y- and HREE-rich (up 1.54 wt% Y; up ~1 wt% ΣREE), and the Y+REE enter the garnet structure via the menzerite-(Y) substitution. The Y and REE show complex zoning patterns and represent sensitive indicator of garnet evolution, in contrast to a rather homogeneous distribution of major divalent cations. General outward decrease of Y+REE is a common feature due to the strong partitioning of Y+HREE in the garnet relative to the other phases. REE underwent significant fractionation during growth of early garnet I; the Yb_N/Nd_N ratio generally decreases from the core to rim of garnet I. Higher Mn and Al, lower Ca, and Y+REE contents, as well as higher Yb_N/Nd_N ratio and more negative Eu anomaly in garnet II overgrowths indicate its crystallization from a more evolved melt. Application of zircon saturation geothermometry provides upper temperature limit of 734 ± 14 ^oC for the closed-system crystallization. Mineral equilibria reveal that crystallization started at QFM + 1.2, and prefential sequesteration of Fe^{3+} into garnet and magnetite was responsible for progressively reducing conditions. Equilibrium between magnetite, garnet, quartz and plagioclase, representing the final crystallization stage of the granitic magma, occurred at 658-663 ^oC and QFM 0 to + 0.8, hence at undercooling of ~75 ^oC.

Key words: garnet; EMP; LA-ICP-MS; Y+REE mass-balance calculations; A-type granite; Brno Batholith

INTRODUCTION

Magmatic garnet (almandine-spessartine) occurs mainly in granitic pegmatites, aplites and felsic peraluminous S-type granitoids (e.g. Allan and Clarke 1981; Miller and Stoddard 1981; Černý and Hawthorne 1982; Deer et al. 1982; Du Bray 1988; Harrison 1988; Dahlquist et al. 2007; London 2008; Sheibi et al. 2010; Müller et al. 2012); it is rare in A-type (Zhang et al. 2009, 2012) or I-type (Wu et al. 2004) granites. Garnet is a useful indicator of changing magmatic conditions during its crystallization and peritectic reactions (e.g. Dahlquist 2001; Wang et al. 2003a; Dahlquist et al. 2007; Erdmann et al. 2009; Lackey et al. 2012). It has also been identified as an important carrier of Y+HREE (Jaffe 1951; Dudykina 1959; Vorma et al. 1966; Wakita et al. 1969; Grew et al. 2010; Marsh et al. 2012) with up to ~3 wt% Y+HREE in magmatic garnets (Wang et al. 2003a), and with up to ~13 wt% Y in metamorphic garnets (Grew et al. 2010; Marsh et al. 2012). The compositional zoning of Y+REE as a sensitive indicator of garnet growth and crystallization history has been recently discussed particularly in metamorphic rocks (e.g. Hickmott and Shimizu 1990; Lanzirotti 1995; de Lima et al. 1995; Spear and Kohn 1996; Bea et al. 1997; Holten et al. 1997; Kotková and Harley 1999; Pyle and Spear 1999; Hermann and Rubatto 2003; Kohn 2004; Čopjaková et al. 2005; Borghi et al. 2006; Buick et al. 2006; Røhr et al. 2007; Spry et al. 2007; Marsh et al. 2012). By contrast, there are only a few studies dealing with Y+REE zoning texture in magmatic garnets (Sevigny 1993; Whitworth and Freely 1994; Wang et al. 2003a; Dorais and Tubrett 2012; Müller et al. 2012) and evolution of Y+HREE/LREE ratios during garnet growth (Sevigny 1993; Dorais and Tubrett 2012).

We describe complexly zoned garnet with Y+REE-enrichment from microgranite portions of subaluminous A-type Hlína granite in order to better understand: (i) the distribution of Y and

69 REE in garnet, (ii) the substitution mechanisms of these elements, and (iii) the role of garnet in
70 controlling Y+REE content in this magmatic rock in particular. Moreover, contributions of the
71 individual minerals to the Y+REE budget in the granite were calculated and discussed.
72

73 ## GEOLOGICAL SETTING

74 The large Cadomian (Pan-African, 650-550 Ma) Brunovistulian microcontinent is a portion of the
75 Precambrian lithosphere that is located at the eastern margin of the Bohemian Massif and
76 occupies parts of Czech, Austrian and Polish territories (Fig. 1). It consists of three major N-S
77 trending tectonic units of distinct character: (i) an ophiolite belt that crops out in the central part
78 and it divides the Brunovistulicum into (ii) the Slavkov terrane in the NE and (iii) the Thaya
79 terrane in the SW (Finger et al. 2000). The most critical and best exposed portion of the
80 Precambrian basement in central Europe is the Brno Batholith (Finger et al. 2000; Leichmann and
81 Höck 2008). Steep geological, tectonic and geophysical boundaries divide the Brno Batholith into
82 three different N-S oriented units mirroring the zoned structure of the whole Brunovistulicum
83 (Fig. 1). These units are (from west to east): the Western Granitoid Complex (WGC, as part of
84 the Thaya Terrane), the Central Ophiolite Belt (COB) and the Eastern Granitoid Complex (EGC,
85 as part of the Slavkov Terrane). The Central Ophiolite Belt (COB; dated at 725 ± 15 Ma by
86 Finger et al. 2000) originated in supra-subduction environment (Finger et al. 2000; Kalvoda et al.
87 2008; Leichmann and Höck 2008), but was subsequently intruded by younger (600-580 Ma)
88 granitoids (WGC and EGC).

89 Three granitic suites were distinguished within the WGC by Leichmann and Höck (2008): (i) the
90 Tetčice (S-type) suite, (ii) the Réna (I-type) suite, both represent evolved rocks of an active
91 continental margin, and (iii) the examined Hlína (A-type) suite (Fig. 1). The Tetčice suite consists

of biotite granite with frequent xenoliths of biotite-amphibole diorites and of metasedimentary rocks. Zircon morphology and alumina saturation index (ASI) = 1.14-1.20 suggest S-type granite affinity (Leichmann and Höck 2008). The Réna suite consists of felsic (SiO_2 > 69 wt%, ASI < 1.1), I-type amphibole–biotite granodiorites to biotite granites interpreted as volcanic-arc products (Leichmann and Höck 2008). Numerous small (tens to hundred meters) and irregular bodies and dykes of the Hlína suite intruded I-type granites of the Réna suite and, less frequently, S-type granites of the Tetčice suite (Fig. 1). Recent mapping (Hönig et al. 2012) confirmed their frequent occurrence in the SW part of the Brno Batholith and within the NE part of the Thaya Batholith (Fig. 1), where the Hlína suite spreads out more than 80 km in north-south direction. The strike of the bodies is generally parallel to the NW-SE trending regional fault zone. Both hanging wall and foot wall contacts of the Hlína granite bodies with the host granodiorite are sharp. The Hlína suite consists of felsic, garnet-bearing leucogranite with anorogenic, post-collisional affinity, and often showing complex internal structure (Hönig et al. 2010).

ANALYTICAL METHODS

Sampling and modal counting

Samples of the A-type Hlína granite for whole-rock chemical analysis and EMP study were collected at 4 localities (A to D in Fig. 1). The detailed EMP and LA-ICP-MS study combined with Y+REE mass balance calculations were performed using the samples of microgranitic units from the granite dyke at the locality A (Moravské Bránice; Fig. 1). Twenty thin sections from this locality were studied in detail using conventional petrographic methods including modal counting.

EMP

Garnet and other rock-forming and accessory minerals from the A-type Hlína granite were analysed with a Cameca SX100 electron microprobe at the Joint Laboratory of Electron Microscopy and Microanalysis, Department of Geological Sciences, Masaryk University, Brno and Czech Geological Survey. Operating conditions for analyses were as follows: wavelength dispersive mode, an accelerating voltage of 15 kV, a beam current of 40 nA for garnet, 20 nA for magnetite and other accessory minerals and 10 nA for muscovite and feldspars; a beam diameter of 2 μm for garnet and accessory minerals, and 5 μm for muscovite and feldspars. The Y+REE in the zircon were analyzed at 150 nA. The P and Sr in feldspars were analyzed at 100nA. The element concentrations in silicate minerals were analysed using the following standards and X-ray lines: K_α lines - sanidine (Si, Al, K), albite (Na), pyrope (Mg), andradite (Ca, Fe), spessartine (Mn), titanite (Ti), chromite (Cr), fluorapatite (P), topaz (F), L_α lines - YAG (Y), Yb ($YbPO_4$), Er ($ErPO_4$), $SrSO_4$ (Sr), baryt (Ba). For magnetite the following standards and X-ray lines were used: K_α lines - $MgAl_2O_4$ (Mg, Al), hematite (Fe), chromite (Cr), titanite (Ca, Ti), Ni_2SiO_4 (Ni), $ScVO_4$ (V), sanidine (Si), Mn_2SiO_4 (Mn); L_α line - gahnite (Zn). The peak counting time was 10 seconds for major elements and 20-80 seconds for minor to trace elements. Average detection limits in garnet are: for Y (340 ppm), Er and Yb (970 and 790 ppm, respectively). The calculated relative errors (2σ error) are about <3 % at the >10 wt% level, <5 % at the ~5 wt% level and <15 % at the ~1 wt% level. Analytical conditions and standards used for zircon and REE-bearing phases were similar to those described by Breiter et al. (2009) and Čopjaková et al. (2011). Chemical analyses of garnet were recalculated to the formula $^{XII}X_3{}^{VI}Y_2{}^{IV}T_3O_{12}$ on the basis of Σ cations = 8 and the Fe^{3+}/Fe^{2+} ratios were calculated by charge balance.

137

138 **LA-ICP-MS**

139 Trace element contents in major (plagioclase, K-feldspar, quartz) and minor to accessory
140 minerals with a grain-size greater than 25 μm (garnet, magnetite, muscovite, epidote) were
141 investigated by LA-ICP-MS (CEITEC and Department of Chemistry, Faculty of Science,
142 Masaryk University, Brno) using an Agilent 7500ce (Agilent Technologies) quadrupole ICP-MS
143 with an attached UP 213 laser ablation system (New Wave Research). The samples were ablated
144 using a commercial Q-switched Nd:YAG laser operated at a wavelength of 213 nm (pulse
145 duration of 4.2 ns). Ablated material was transported from the sample chamber using helium
146 carrier gas (1 L/min) and mixed with argon (0.6 L/min) prior to the torch. Optimization of LA-
147 ICP-MS parameters (gas flow rates, sampling depth, voltage of ion optics) was performed using
148 glass reference material NIST SRM 612 to maximize the S/N ratio and minimum oxide formation
149 (ThO^+/Th^+ counts ratio 0.2 %) and U^+/Th^+ counts ratio 1.1 %. Potential polyatomic interferences
150 were minimized by collision reaction cell in He mode (2.5 mL/min).

151 The contents of major and trace elements in garnet, magnetite, muscovite, epidote, plagioclase
152 and K-feldspar were determined after laser ablation of individual spots with various diameter
153 (garnet - 55 μm; magnetite - 80 μm; muscovite - 40 μm; epidote - 25 μm; plagioclase and K-
154 feldspar - 110 μm) and fluence of laser beam (garnet, magnetite and plagioclase - 5 $J.cm^{-2}$;
155 muscovite, epidote and K-feldspar - 3 $J.cm^{-2}$) depending on the size of analyzed grains. Analyses
156 of mineral samples were carried out at frequency of 10 Hz and each spot was ablated for 60 s.
157 The element content in quartz sample was traced by line scanning mode at the diameter of 65 μm
158 and 5 $\mu m.s^{-1}$ scan speed. The fluence of laser beam was set to 20 $J.cm^{-2}$ and the analysis was
159 carried out at frequency of 5 Hz. The contents of elements of interest were estimated using SRM

NIST 610 and 612 and internal reference element (Si – silicates, Fe – magnetite). The calculation was performed after baseline correction and integration of peak area.

Whole rock chemical analyses

Whole rock chemical analyses (8 samples) were determined at the Acme Chemical Laboratories Ltd, Vancouver, Canada. Major elements were determined by using ICP-OES after fusion with lithium borate flux. Trace elements, including the REE, were analyzed by ICP-MS with additional lithium tetraborate fusion.

PETROGRAPHIC DESCRIPTION AND GEOCHEMISTRY OF THE HLÍNA GRANITES

Internal structure and petrography

The Hlína granite bodies show relatively complex internal fabric. The intrusions are predominantly built by fine-grained leucocratic microgranite with layering defined by large proportion of garnet trains parallel to the contacts (Fig. 2; the train texture is used to characterize garnets arranged into the subparallel strips, where individual garnet crystals are almost in a direct contact with each other; e.g. Bogoch et al. 1997; Macleod 1992). The garnet trains are up to several millimeters thick layers or layer sequences within the microgranite portion of the body. In some cases the microgranite is interlayered with comb-shaped large crystals of K-feldspar, plagioclase and quartz (more than 10 centimeters large) designated as unidirectional solidification textures, UST (Shannon et al. 1982; for more detail see Hönig et al. 2010). The USTs are developed mostly in marginal and apical parts of the intrusions and are parallel to the intrusive

contacts (Fig. 2a). Alternations of the garnet-bearing microgranite and garnet-free UST layers extend over several meters within some of the Hlína bodies.

The fine- to medium-grained (0.5 to 2 mm) microgranite is composed of plagioclase An_{8-15} (35-45 vol%), K-feldspar (23-30 vol%) and quartz (20-32 vol%). The common minor to accessory minerals are muscovite (3-5 vol%), garnet and magnetite (<2 vol%). Other accessory minerals: epidote > zircon > ilmenite > secondary REE-bearing phases >>> titanite > Nb-Ta oxides > xenotime-(Y) are rare to extremely rare. The grain size of the UST zones varies from 1 to 10 cm. The mineral assemblage is represented by K-feldspar, plagioclase (An_{10-15}) and quartz with minor muscovite; accessory minerals are extremely rare or absent.

Garnet

Garnet is present in two distinct morphological types: (i) the most abundant euhedral garnet (<0.5 mm) is arranged in long trains (from several dm to several m long; Fig. 2). These trains locally alternate with similar but less abundant zones of individual magnetite grains. Euhedral garnet is commonly inclusions-free (Fig. 3a-c); but it rarely encloses magnetite or minute zircon grains; (ii) rather rare glomerophyric garnet (enclosing K-feldspar, quartz, plagioclase) forms isolated phenocrysts (0.5-4 mm) with no apparent spatial relation to the garnet trains (Fig. 3d).

The euhedral garnet exhibits complex zoning patterns in BSE images characterized by core with pronounced sector zoning usually overgrown by zones with sharply-defined fine oscillation – garnet I (Fig. 3a-c). Both texturally distinct domains of garnet I, that is, volumetrically minor sector zoned cores and volumetrically dominant domain with oscillatory zoning, show similar chemical composition with gradual changes in major and trace elements. The euhedral garnet I

corresponds to $Sps_{45–46}Alm_{27–38}And_{4–13}Grs_{0–12}Mzr_{2-5}Prp_{0–1}$ (Fig. 4a; Table 1). Major cations (1.27-1.36 apfu Mn, 1.13-1.27 apfu Fe, molar $Mn/(Fe_{tot}+Mn)$ ratio = 0.50-0.52) are rather constant and display negligible variations across garnet I grains (Fig. 4b). Garnet I shows low Al (1.63-1.84 apfu), but it is enriched in Fe^{3+} (0.09-0.26 apfu) and particularly in Ca (0.49-0.70 apfu). The contents of Al and Fe^{2+} (0.90-1.18 apfu) gradually increase, whereas Fe^{3+} decreases from the core outwards with no discontinuity during transition from sector to oscillatory zoned domain (Fig. 4b). The content of Ca is constant through the central part of the garnet and depleted in its outer part. The content of Mg (0.03-0.06 apfu) decreases slightly from the core outwards. Along with Y (0.03-0.09 apfu; 0.61-1.96 wt% Y_2O_3), other HREE were detected by EMPA ($Er_2O_3 \leq 0.30$ wt%, $Yb_2O_3 \leq 0.57$ wt%). The contents of Y+HREE generally decrease from the core outwards (Fig. 4b), but in detail their values finely oscillate and correlate well with the zoning observed in the BSE images (Fig. 4c). The content of Ti is rather high (≤ 0.44 wt% TiO_2) and it is negatively correlated with Al. The content of Na_2O does not exceed 0.16 wt%.

Recalculation of the end-members in euhedral garnet shows rather constant spessartine, increase of almandine and decrease of andradite from the core outwards. The content of the grossular end-member increases generally from the core outwards and the Y+HREE content display the opposite behavior (Fig. 4b).

In some of the garnet-bearing granite samples, the outermost parts of some garnet I crystals were locally overgrown or replaced by later garnet II (Fig. 3b,c). The replacement irregularly propagates from the rim inwards and the boundary between garnet I and garnet II is texturally and chemically sharp. The later garnet II is slightly enriched in Mn, Al and Fe^{2+} and depleted in Ca, Y+HREE, Fe^{3+} and Ti compared with the garnet I (Fig. 4; Table 1).

The rare glomerophyric garnet is only slightly enriched in andradite and spessartine and depleted in almandine and grossular ($Sps_{44–46}Alm_{28–38}And_{6-15}Grs_{6–10}Mzr_{0-4}Prp_{0-1}$) when compared to the euhedral garnet (Fig. 4a; Table 1). The contents of Y (0.01-0.07 apfu; 0.19-1.59 wt% Y_2O_3) and HREE ($Er_2O_3 \leq 0.30$ wt%, $Yb_2O_3 \leq 0.45$ wt%) in the glomerophyric garnet are similar to those in the euhedral garnet. The compositional profile through glomerophyric garnet shows similar chemical zoning as the euhedral garnet.

Other rock-forming and accessory minerals

Pink subhedral crystals of K-feldspar ($Or_{81}Ab_{17}An_{0.5}$) show two or more crosscutting perthitic systems. Plagioclase ($An_{8–15}$) is simply zoned with typical magmatic zoning trend with more calcic core and a myrmekitic texture commonly developed along the contacts with K-feldspar. Both K-feldspar and plagioclase have low concentrations of P (≤0.01 wt% P_2O_5); low Sr abundances (≤0.08 wt% SrO) in plagioclase are typical.

Muscovite forms rather anhedral small flakes. It is Fe-rich (Fe_{tot} up to 0.45 apfu) with Si up to 3.23 apfu, and Al ~2.3 apfu. Low contents of Na (≤0.03 apfu), Mg (≤0.04 apfu) and F (≤0.04 apfu) are typical. Muscovite is partly replaced by chlorite (chamosite with Fe/(Fe+Mg) = 0.70-0.97). Wormy epidote (0.71-0.88 apfu Fe^{3+}) intergrowing with quartz usually overgrows muscovite or magnetite. Euhedral crystals of magnetite (20-300 μm) are close to the ideal composition with only trace amounts of Ti, Al and Si.

Euhedral to subhedral crystals of zircon (5-50 μm) are remarkably altered (Fig. 3e). Relics of relatively "fresh" zircon (Zr/Hf = ~19) are very rare and contain only low concentrations of P (≤ 0.33 wt% P_2O_5), $(Y,REE)_2O_3$ (up 1.4 wt%), U (0.12-1. 50 wt% UO_2), and Th (0.05-0.30 wt%

247 ThO_2). On the other hand, altered domains (Table 2) are depleted in SiO_2 (17.11-27.27) and ZrO_2
248 (38.21-52.08 wt%) and enriched in P_2O_5 (1.59- 6.77 wt%), Nb_2O_5 (0.08 - 3.57 wt%), CaO (0.24-
249 1.67 wt%), ThO_2 (0.21 - 28.19 wt%), UO_2 (0.23 - 2.39 wt%), FeO (0.76 - 3.93 wt%), Al_2O_3
250 (0.75-3.76 wt%) and $(Y,REE)_2O_3$ (2.94 - 9.72 wt%). The low sum of oxides (83-93 wt%) and the
251 presence of non-essential elements (Fe, Ca, Al, Nb, F) suggests amorphous and hydrated nature
252 of the altered parts of zircon. Incorporation of these elements into the amorphous zircon during
253 interaction with hydrothermal fluids was documented, for instance, by Geisler et al. (2003, 2007).
254 The chondrite-normalized REE pattern of the zircon is HREE-enriched; nevertheless, in the
255 altered parts it is rather flat (Yb_N/Nd_N = 10-15) with a weak positive Ce anomaly (Fig. 5a).
256 Aggregates of secondary REE-bearing phases and clay minerals (10-70 μm large) occur
257 sporadically in thin sections, they follow primary grain boundaries or radiation damage haloes
258 (Fig. 3g,h). Needle-like REE-bearing secondary phase corresponds to Th-rich rhabdophane-(Nd)
259 (0.06-0.23 apfu Th) with variable negative Ce anomaly (Ce/Ce* = 0.1-0.6; Fig. 5a), and with
260 0.07-0.12 apfu Y (Table 2). Another secondary phase is uranium-rich (up 6.5 % UO_2; Fig. 3g,h)
261 and it show very low REE contents close to the detection limit of EMP excluding Ce, yielding
262 significant positive Ce anomaly (Ce/Ce* ~4; Fig. 5a). Xenotime-(Y) forms sporadically
263 pyramidal overgrowths on the zircon crystals. Other accessory minerals (fersmite, columbite-
264 (Fe), plumbopyrochlore and titanite) are extremely rare, with the contents of Y+REE below the
265 detection limit of EMP.

266

267 **Whole rock chemistry**

268 The felsic character of all samples (SiO_2 74.61-75.86 wt%, K_2O 4.11-4.94 wt%, Na_2O 3.82-4.94
269 wt%) is consistent with the high-K calc-alkaline and a metaluminous to slightly peraluminous

nature (ASI = 0.98-1.08). Moderate concentrations of CaO (0.61-1.20 wt%), and low concentrations of Fe_2O_{3tot} (0.62-0.93 wt%), MgO (0.02-0.03 wt%), TiO_2 (0.03-0.04 wt%) and P_2O_5 (0.01-0.05 wt%) indicate a generally evolved character of these rocks (Table 3). Rather high concentrations of MnO (0.04-0.90 wt%), Rb (156-311 ppm) and Nb (11-51 ppm) are typical for garnet-enriched rocks and positively correlate with high contents of Y (14-116 ppm) and HREE (Yb 4-15 ppm, Er 2-11 ppm). Compared to the granites of the Réna and Tetčice suites (Leichmann and Höck 2008), the contents of Zr (66-107 ppm), Sr (13-30 ppm), and Ba (4-46 ppm) are low. Low K/Rb (110-241), fairly low mg# 4-7 (defined as molar ratio of 100 MgO/(FeOt+MgO)), strong negative Eu anomaly ($Eu/(Sm \times Gd)^{1/2}$ = 0.15-0.36) and very high K/Ba (742-2544) indicate a high degree of fractionation. The rock is depleted in LREE (only ~10 times enriched over chondritic abundances) relative to HREE (70-90 times enrichment relative to chondrite), the La_N/Yb_N ratios vary from 0.53 in garnet-free rocks to 0.13 in garnet-rich zones (Fig. 5f). The Hlína suite falls mostly into the field of within-plate granites (Fig. 6a,b) and, according to the Ga/Al ratio (Fig. 6c), the rocks plot into the field of A-type granites. Based on the concentrations of Y, Nb and Ga*3 (Fig. 6d) the Hlína granites are classified as the rocks with a post-collision, post-orogenic and anorogenic affinity.

LA-ICP-MS DATA

Garnet

Yttrium and REE were measured across 10 crystals of euhedral garnet, 3 to 11 analyses were obtained along each analytical profile (total 72 analytical points). Yttrium contents vary from 2630 to 15530 ppm. Total rare earth element concentrations vary from 1710 to 9990 ppm and positively correlate with Y contents (Table 4). The concentrations of the Y, Yb and Er obtained

by LA-ICP-MS are in good agreement with the results of EMPA. All analyses show enrichment in HREE (Yb_N/Sm_N = 17-441) and significant Eu anomaly (Eu/Eu* = 0.01-0.05; Fig. 5b; Table 4). The Yb_N/Sm_N ratio decreases smoothly with decreasing ΣY+REE contents from core towards the rim of the garnet I (Fig. 7a) with no disruption during transition between domains with sector and oscillatory zoning. By contrast, garnet II shows significantly higher Yb_N/Sm_N compared with the outer zones of garnet I (Fig. 7a,b). Moreover, garnet II has more negative Eu anomaly compared with garnet I (Fig. 7c,d).

Other rock-forming and accessory minerals

The Y+REE contents in magnetite are relatively high (90-256 ppm; Table 4). Chondrite-normalized REE patterns (Fig. 5c) are nearly flat (La_N/Yb_N = 0.4-2.7) with a significant negative Eu anomaly (Eu/Eu*=0.10-0.15) and a negative Ce anomaly (Ce/Ce* = 0.47-0.77). The Y+REE concentrations in primary muscovite are rather low (8-95 ppm; Table 4). The chondrite normalized REE patterns (Fig. 5d) are flat to slightly LREE-enriched (La_N/Yb_N=0.5-5.3), with a negative Eu anomaly (Eu/Eu*=0.22-0.77) and a positive Ce anomaly (Ce/Ce*=0.93-4.94). The highest □Y+REE contents (□26 ppm) in muscovite correlate with increased contents of Nb and Ta and could indicate presence of submicroscopic inclusions of Y+HREE-rich Nb- and Ta-containing phases. The Y+REE in plagioclase range from 1.0 to 6.7 ppm; the LREE (0.6-4.0 ppm) predominate over HREE (0.08-1.4 ppm), and there is a distinct positive Eu anomaly (Eu/Eu* = 1.9-10.5; Fig. 5e; Table 4). K-feldspar (Y+REE = 0.6-3 ppm) has only the LREE significantly above the detection limit and positive Eu anomaly. The HREE are close to or below the detection limit (Fig. 5e; Table 4). The Y+REE contents in quartz are low and close to the chondritic values (Y+REE = 3-11 ppm), with flat Ce_N/Yb_N ratio close to 1 (Table 4). and.

316 Epidote has low contents of LREE (Σ LREE ~10-30 ppm) with a steep LREE-rich chondrite
317 normalized pattern (HREE are below the detection limit) and a weak negative Ce anomally (Fig.
318 5d; Table 4).

319

320 ## MINERAL MASS BALANCE FOR Y+REE

321 ### Mineral mass calculation

322 The Y+REE mineral mass-balance calculations for three granite samples (MB1-1, MB1-52 and
323 MB1-55; Fig. 5f; Table 3) were carried out in order to assess the relative contribution of garnet
324 and other rock-forming minerals to the whole-rock Y+REE budget. These calculations ignore
325 rare small accessory minerals (<10 μm) with Y+REE contents below the detection limit of EMP
326 (ilmenite, titanite, Nb-Ta oxides) and extremely rare xenotime (one 5 by 10 μm-large xenotime-
327 (Y) grain per thin section contributes less than 0.05 % of the total Y+REE in granite). The
328 proportional contents of quartz, K-feldspar, plagioclase, muscovite and garnet were calculated by
329 mass balance using average EMP data and whole rock chemical compositions. The garnet
330 fraction was calculated from the MnO content in the whole rock lowered by the MnO content
331 retained in muscovite, magnetite and ilmenite. The magnetite, ilmenite and epidote fractions were
332 calculated using BSE image analysis. The fraction of zircon was calculated from the Zr content in
333 the rock lowered by the total Zr content located in other rock-forming minerals. The Y+REE
334 mass-balance calculations were performed as arithmetic mean of the Y+REE in individual
335 minerals (excluding garnet) and their modal content in the rock. Average Y+REE contents for
336 garnet could not have been calculated from the rim-core-rim profiles of the LA-ICP-MS analyses
337 as arithmetic mean because this approach would provide significantly higher Y+REE budget (in
338 this case 1.24 times higher than spherical layer model) due to significant core-rim zoning in

339 Y+REE. Thus, the average Y+REE content of the garnet was calculated by the spherical layer
340 model (see Fig. 3f). The calculated Y+REE budgets are presented in Tables 5 and 6 and
341 graphically in Fig. 8.

342

343 **Distribution of Y+REE among rock-forming minerals**

344 The mineral mode and average Y+REE contents in individual primary minerals (garnet, zircon,
345 muscovite, magnetite, quartz, plagioclase, K-feldspar, epidote) were used to calculate the
346 theoretical Y+REE pattern of the whole rock (model A). The calculated Y+REE pattern of the
347 model A is in a good agreement with the pattern obtained from the whole-rock analysis (Fig. 8a)
348 excluding LREE from La-Sm. Due to the strongly heterogeneous chemical composition of
349 aggregates of secondary REE-bearing phases their modal amount was difficult to determine.
350 Therefore, the fraction of secondary REE-bearing phases was calculated according to the
351 unbalanced La-Sm content between the model A and the whole rock chemical analysis and
352 average chemical composition of the secondary REE-bearing phases. The mode of secondary
353 phases corresponds to 10 grains, ~50 μm in size, per thin section, which seems to be consistent
354 with the observations of secondary REE-bearing phases in our samples. Model B (Fig. 8a)
355 expresses a theoretical Y+REE pattern obtained by addition of the secondary REE-bearing phases
356 to the model A. The difference between these two models suggests that ~63 % of the whole rock
357 LREE budget is hosted by secondary REE-bearing phases, which also contribute 1 % to the
358 whole rock Y and 21 % to the whole rock REE.

359 The results shown in Table 5 demonstrate that ~84 % of the Y and ~61 % of the REE are hosted
360 in garnet. The garnet contribution to the HREE is ~86 % and it systematically increases from Gd
361 to Yb (Fig. 8b; Table 6). Zircon, the second important carrier of Y+REE in the rock (Fig. 8b;

Table 5), contains ~13 % of whole rock Y and ~11 % REE (11 % LREE and 11 % HREE). The fraction of Y+REE residing in the major rock-forming minerals (plagioclase, K-feldspar, quartz), is with the exception of Eu rather low ~1 % Y and 4 % REE (of 10 % LREE and 1 % HREE) despite the predominance of these minerals (94 vol%) in the rock. Approximately 89 % of Eu is contained in feldspars (Fig. 8b; Table 6). Surprisingly, a relatively high content of Y+REE in magnetite makes it a relatively important reservoir of Y (1 %) and REE (2 % of the total REE and 4 % of the total LREE), despite its low modal amount (Table 5). Moreover, ~1 % Y and 2 % REE (4 % LREE>0.5 % HREE) reside in muscovite (Table 5). The contribution of epidote to the Y+REE whole rock budget is only negligible (0.3 % of the total LREE; Table 5).

DISCUSSION

Crystallization temperature

We have used the zircon saturation thermometry to evaluate the liquidus temperature of the Hlína A-type granite. Application of the zircon solubility model in silicate melts (Harrison and Watson 1983) yields temperature range between 711-751 ^{o}C, that is, 734 ± 14 ^{o}C. The zircon saturation thermometry is applicable provided that Zr remained immobile on the sample scale during postmagmatic alteration of zircon. Several lines of evidence suggest its generally conservative behavior: (i) the Zr concentrations in six whole rocks neither correlate with the degree of zircon alteration nor they show irregular fluctuations, (ii) the estimated temperatures are not scattered but form a rather narrow range, and (iii) if portion of Zr was removed by aqueous fluids, the original crystallization (saturation) temperature would have to be higher than ~730 ^{o}C, which is unexpected for highly evolved granitic magmas (e.g., Anderson et al. 2008; Huang and Audétat

2012; London 2014). We thus interpret results of the zircon saturation thermometry as maximum liquidus temperature, and subsequent crystallization must have proceeded in a closed system.

The minimum temperature limit of granite crystallization was estimated by two-feldspar solvus geothermometry using non-ideal asymmetric mixing model of Holland and Powell (2003). K-feldspar composition exhibits slight systematic decrease in Na concentrations from core to rim (Ab_{14-09} to Ab_{05-04}). Plagioclase composition shows minor but systematic decrease from An_{15} to An_{14-12} (core to rim), with Or_{00-01}. Cores of corresponding plagioclase and K-feldspar grains indicate equilibrium temperatures from 441 ± 14 to 418 ± 18 ^{o}C at 1 kbar. By contrast, rims of plagioclase and K-feldspar grains yield variable, poorly constrained temperatures from 413 ± 97 to 294 ± 15 ^{o}C at 1 kbar. We interpret the range of 441-418 ^{o}C as a minimum temperature limit for granite crystallization, possibly under undercooled conditions, whereas the latter datum of 294 ± 15 ^{o}C is appears to indicate closure of the Na-K exchange *via* grain boundary diffusion. Layered textures (alternating garnet-bearing aplite and garnet-free coarse-grained comb-like UST layers) observed in the Hlína granite together with hour-glass sector cathodoluminiscence-zoning of K-feldspar and sector zoning in central parts of the garnets indicate a crystallization from non-equilibrium supersaturated undercooled melt (*cf.* Webber et al. 1999; London 2009, 2014; Hönig et al. 2010), broadly bracketed by 734 and 441-418 ^{o}C.

Igneous origin of garnet

The origin of garnet in granitic magmas (magmatic phenocrysts, xenocrysts, restite or secondary reaction products) is still intensively debated (e.g. Miller and Stoddard 1981; Kontak and Corey 1988; Hogan 1996; Dahlquist et al. 2007; Erdmann et al. 2009; Dorais and Tubrett 2012; Lackey et al. 2012). The chemical composition and zoning, euhedral morphology (Figs. 3a-c, 4) and

407 textural relations of garnet from the Hlína granite are consistent with its igneous origin. Garnet I
408 crystallized early from the felsic magma that was highly evolved, metaluminous to weakly
409 peraluminous (ASI = 0.98-1.08; Table 3) and rich in Y+HREE, Mn and poor in Mg, P, and Eu.
410 By contrast, formation of garnet in response to a biotite-consuming reaction, which would have
411 reflected an increase in the melt peraluminosity due to the progressive crystallization (Hogan
412 1996), appears to be unlikely. Interstitial, rather anhedral primary muscovite and wormy epidote
413 crystallized later, when H_2O concentration in the residual melt increased slightly, and this is
414 consistent with mineral sequences observed in A-type magmas crystallizing under initially low
415 H_2O fugacities (e.g. Bonin 2007).

416 The excess of Al in the melt is usually considered to be a prerequisite for garnet stability (du
417 Bray 1988). This is in agreement with common occurrence of accessory garnet of almandine-
418 spessartine composition with low contents of Mg and Ca (<2 wt% CaO) in the S-type (ASI □
419 1.1) granites. Commonly, such garnets are Al-rich (1.95-2.00 apfu Al; Miller and Stoddard 1981;
420 du Bray 1988; Sevigny 1993; Dahlquist et al. 2007; Sheibi et al. 2010). By contrast, magmatic
421 garnet in the A-type Hlína granites shows lower Al concentrations (~1.6 apfu in garnet cores),
422 which are compensated by Fe^{3+} ± Ti in the octahedral site (Fig. 4b; Table 2). The decreased Al
423 and elevated Ca, Fe^{3+} and Ti concentrations in garnet enable garnet crystallization from weakly
424 peraluminous melt (with ASI ~1). The garnet I composition resembles those described from
425 highly fractionated metaluminous to weakly peraluminous (ASI = 0.96-1.05) A-type granites at
426 Erlangmiao (Zhang et al. 2012).

427 Chemical composition (both major and trace elements) indicates that the transition from sector
428 zoned cores of garnet I to oscillatory zoned garnet I domains reflects continuous garnet
429 crystallization with no disruption in garnet growth (Fig. 4b, 7). Sector-zoned cores of garnet I

crystallized rapidly from undercooled melt far from equilibrium with coexisting minerals. Moreover, rim of oscillatory zoned garnet I crystallized close to equilibrium with coexisting minerals. Flat Mn and Fe_{tot} profiles (Fig. 4b) for garnet I could reflect rapid self-diffusion of these elements, which is characteristic for garnets that have crystallized at high temperatures ~ 700 °C (Yardley 1977; Manning 1983; Harrison 1988; Dahlquist et al. 2007). This observation agrees well with the results of the zircon saturation geothermometry and confirms that garnet I is an early, high-temperature liquidus phase in A-type granitic magmas (Bonin 2007).

Redox conditions during crystallization

We used the composition of garnet I (from a sample with no other garnet varieties present), in combination with that of other coexisting minerals, to reconstruct the redox conditions during magma crystallization (Fig. 9). The following mineral equilibria are applicable to garnet- and magnetite-bearing leucogranites:

$$3\ \text{skiagite} + 1\ O_2 = 5\ \text{magnetite} + 9\ \text{quartz} \quad (1)$$

$$9\ \text{grossular} + 4\ \text{magnetite} + 9\ \text{quartz} + 1\ O_2 = 6\ \text{andradite} + 9\ \text{anorthite} \quad (2)$$

We used the internally self-consistent thermodynamic dataset of Holland and Powell (1998), as updated in 2004, the compensated Redlich-Kwong equation of state for H_2O (Holland and Powell 1991, 1998) and the asymmetric non-ideal mixing models for plagioclase (Holland and Powell 2003) and garnet (White et al. 2007, as revised by Diener et al. 2008 and incorporating ideal Fe-Mn mixing in the sense of White et al. 2005) to evaluate redox conditions of these equilibria with

452 respect to fayalite or anthophyllite-magnetite-quartz and magnetite-hematite oxygen-fugacity
453 buffers. Thermodynamic data for the skiagite end-member ($Fe_3Fe_2Si_3O_{12}$) were calibrated by
454 Malaspina et al. (2009), however, their exploratory application indicated equilibrium redox
455 conditions in excess of the magnetite-hematite buffer, in a strong disagreement with the observed
456 mineral assemblage and outside the range of common igneous rocks (e.g., Carmichael 1991,
457 Frost and Lindsley 1992). We prefer to estimate the thermodynamic data for the skiagite end-
458 member from the reciprocal composition space of the garnet solid solution in a self-consistent
459 manner with non-ideal excess mixing contributions (Diener et al. 2007).

460 Eq. (1) applied to the composition of garnet I core (sector zoned domain of the garnet I) yielded
461 log fO_2 = -14.9 bar (Fig. 9), which corresponds to QFM + 1.2 at 734 ^oC (zircon saturation
462 temperature). Progressive crystallization of Fe^{3+}-bearing garnet I decreases the Fe^{3+}/Fe^{2+} ratio of
463 the residual melt, thus effectively shifting the evolving system towards more reducing conditions.
464 The equilibrium between garnet I rim (homogeneous rim of oscillatory zoned domain of the
465 garnet I), magnetite and quartz yielded log fO_2 = -16.2 bar at 718 ^oC, which is the liquidus
466 temperature for the crystallization of garnet and magnetite, as opposed to stability of garnet and
467 fayalite at lower temperatures. The equilibrium between quartz, magnetite, plagioclase and rim of
468 garnet I was reached at 657 ^oC as indicated by the intersection of Eq. (2) with the QFM buffer,
469 whereas the equilibrium between the same phase but garnet II occurred under similar conditions,
470 at 663 ^oC and QFM + 0.8 (Fig. 9). The location and course of the garnet-magnetite equilibrium
471 (Eq. 1; Fig. 9) indicate that the garnet I core composition will change only little if the
472 crystallization has occurred metastably during undercooling below ~730 ^oC. Following the
473 crystallization of garnet I, compositional changes of the residual melt caused its temporary
474 instability, it was partly dissolved and overgrown by Ca,Y+REE-poor and Mn,Al-rich garnet II

(Figs. 3b,c, 4b, 7). Despite these compositional fluctuations the compositions of both garnet types yield consistent crystallization conditions, 657-663 ^{o}C and QFM 0 to + 0.8 at 1 kbar, which represent an undercooling of ~75 ^{o}C below the zircon saturation temperature. The estimated redox conditions (QFM 0 to +1.2) indicate that the Hlína suite belongs to moderately oxidized A-type granites (Frost et al. 1999), but are consistent with oxygen fugacity recorded by magnetite, titanite and ilmenite assemblages (Wones 1989), which are all observed in our samples.

Y+REE substitutions in garnet

Four substitution mechanisms controlling incorporation of Y+HREE into the garnet structure have been proposed previously: (i) YAG substitution, $[^{X}(Y,REE)^{3+}{}_{1}{}^{T}(Al^{3+},Fe^{3+})_{1}{}^{X}(R^{2+})_{1}{}^{T}Si_{-1}]$, is considered to be common in spessartine-rich garnets from pegmatites (e.g., Jaffe 1951) and it has been confirmed in metamorphic garnet as well (Røhr et al. 2007); (ii) coupled substitution linked to the incorporation of Na into the X-site $[Na^{+}{}_{1}(Y,REE)^{3+}{}_{1}(R^{2+})_{-2}]$ described by Enami et al. (1995) from metamorphic garnet in orthogneisses; (iii) menzerite-(Y) substitution $^{X}(Y,REE)^{3+}{}_{1}{}^{Y}R^{2+}{}_{1}{}^{X}R^{2+}{}_{-1}{}^{Y}(Al,Fe)^{3+}{}_{-1}$ has been described from metamorphic garnets in felsic granulites only (Grew et al. 2010; Marsh et al. 2012); (iv) $(Y,REE)^{3+}{}_{1}Al^{3+}{}_{-1}$ homovalent substitution for the garnet from the Xihuashan granitic complex (Wang et al. 2003b), although the same trend may be explained by the menzerite substitution (Grew et al. 2010).

The absence of Al in the T-site and negative correlation of Y vs. ^{Y}Al in garnet from the Hlína granites (Fig. 10a) implies the absence of the YAG substitution. Owing to the low Na contents (0.026 apfu) and the lack of correlation with the Y+REE contents (Fig. 10b), only minor contribution from the substitution $^{X}Na^{X}Y^{X}R^{2+}{}_{-2}$ is expected. Yttrium concentrations negatively correlate with $^{X}R^{2+}$ (Fig. 9c), and positively correlate with $^{Y}R^{2+}$ (Fig. 10d). These observations

498 suggest participation of the "ferro-menzerite"-(Y) substitution in garnet from the Hlína granite.
499 Positive correlations of Y and ^{X}Ca and $^{Y}Fe^{3+}$ (Figs. 10e,f) further demonstrated that incorporation
500 of Y into the garnet structure is promoted by the andradite component. Menzerite (or "ferro-
501 menzerite") substitution operates in low-pressure magmatic spessartine-rich garnet (this study)
502 along with high-grade metamorphic rocks (Grew et al. 2010; Marsh et al. 2012).
503

504 **Garnet and further carriers of Y+REE in the rock**

505 The whole-rock budget of Y+REE elements is principally controlled by accessory minerals and
506 their assemblage reflects the ASI and activity of P_2O_5, F and other volatiles (e.g. Bea 1996;
507 Dahlquist 2001; Trumbull et al. 2010). Nevertheless, mineral mass-balance calculations for
508 Y+REE are rather scarce (Ward et al. 1992; Bea et al. 1994; Bea 1996; Dahlquist 2001; Förster
509 and Rhede 2006; Trumbull et al. 2010). In peraluminous granites more than 90 wt% of the
510 whole-rock Y+REE budget reside in the Y+REE-bearing phosphates (monazite, apatite,
511 xenotime) and zircon. The presence of REE-bearing phosphates reflects high phosphorus
512 solubility in peraluminous melts (Ward et al. 1992; Bea et al. 1994; Bea 1996). In metaluminous
513 to weakly peraluminous I-type granites zircon, allanite, titanite with amphibole are the main
514 carriers of Y+REE (Bea 1996; Dahlquist 2001; Trumbull et al. 2010). The sporadic mineral
515 mass-balance calculations for A-type granites indicate that REE-carbonates, allanite, niobo-
516 tantalates and zircon are the main carriers of Y+REE together with minor titanite, xenotime and
517 monazite (Bea 1996).

518 Garnet in peraluminous S-type granites contains only low Y (45-700 pmm) and Σ REE
519 concentrations (40-600 ppm; du Bray 1988; Sevigny 1993; Bea 1996) and therefore hosts only
520 subordinate amounts of the whole-rock Y+HREE budget (Bea 1996). On the contrary, it seems

521 that high Y (≤1.32 wt% Y- Harrison 1988; ≤1.89 wt% Y- Wang et al. 2003b; ≤1.54 wt% Y- this
522 study) and ΣREE contents (≤0.50 wt% - du Bray 1988; ≤1.00 wt% - this study) are common in
523 magmatic garnet found in fractionated SiO_2-rich and P-poor A-type and I-type granites. Low
524 contents of P in the melt prevented precipitation of REE-bearing phosphates in the Hlína granite
525 and the Y+REE remained incompatible in the melt until the saturation in garnet was reached.
526 Garnet is a major carrier of Y and REE in the A-type Hlína granite and accounts for about 84 %
527 of the Y and 61 % of the REE whole-rock budget (Fig. 8b, Table 5,6). Despite rather low ASI in
528 the A-type Hlína granites (Table 3), the allanite is absent and titanite is very rare. This is
529 consistent with its absence in the most siliceous granites elsewhere due to their low Ca contents
530 (Frost et al. 2000). The negligible contribution of epidote to the LREE whole rock budget in the
531 Hlína granite (Fig. 8b) is in contrast to observations from metaluminous granites and mafic
532 metamorphic rocks, where epidote-group minerals can host 50-95 % of LREE regardless of the
533 species (allanite, epidote, zoisite; Bea 1996; Spandler et al. 2003). Epidote in the Hlína granite
534 formed as a late mineral from REE-depleted melt. Spandler et al. (2003) confirmed that garnet
535 represents the dominant host for Y+HREE in metamorphosed pelitic and mafic rocks under
536 epidote blueschist to eclogite facies conditions as well. The REE pattern of zircon is relatively
537 flat, LREE-rich (Fig. 5a) when compared to typical REE patterns in zircon from granitic rocks
538 (cf. Hoskin and Schaltegger 2003). This unusual chemical composition makes zircon an
539 important carrier not only of Y and HREE (13 % Y and 11 % HREE of the whole-rock budget)
540 but also of LREE (11 % of the whole-rock budget; Fig. 8b). This LREE enrichment is probably a
541 result of interaction of amorphous and hydrated zircon-breakdown products with LREE-bearing
542 hydrothermal fluids.

Secondary REE-phases (Figs. 3g,h) represent alteration products after a primary REE-bearing mineral enriched in U and Th, probably Th- and U-rich monazite or cheralite. This primary REE mineral hosted 21 % of REE and 1 % of Y (assuming that REE remained immobile during hydrothermal alteration), and represented important carrier of LREE (63 %) mainly from La to Nd (Fig. 8b; Table 5,6). Trivalent cerium from primary phosphate was probably partly oxidized to Ce^{4+} during the phosphate alteration and the released REE were redistributed between Ce-depleted rhabdophane-(Nd) accommodating REE^{3+} and a Ce^{4+}+U-enriched phase (Fig. 5a).

Only a few attempts have been made to investigate the Y+REE contents of magnetite from granites. Magnetite in the Hlína granite has similar Y+REE content and pattern (Fig. 5c) to the magnetite from the Rostberget granite (Öhlander et al. 1989) excluding the presence of negative Ce anomaly. The negative Ce anomaly in magnetite is accompanied by positive Ce anomaly in zircon and muscovite suggesting that Ce^{3+} was partly oxidized to Ce^{4+} and behaved distinctly from the other REE.

Processes controlling Y+REE variations in garnet

Bulk diffusivities for many trivalent trace elements (including Y+REE) in garnet are slower than those for major divalent (Mg, Fe, Mn) cations or for other octahedrally or tetrahedrally cations (Lyasevich et al. 1977; Yardley 1977; Loomis et al.1985; Chakraborty and Ganguly 1992; Cherniak 1998; Carlson 2006, 2012).

General outward decrease of Y and REE is a common feature of garnet from the A-type Hlína granite (Figs. 4b,c,7), and it is common in garnet from some highly fractionated I-type granites (Wang et al. 2003a) and granitic pegmatites (Smeds 1994; Whitworth and Freely 1994; Müller et

565 al. 2012) as well as from biotite granodiorites (Dorais and Tubrett 2012). In contrast, garnet from
566 peraluminous S-type granites shows increasing Y+REE contents from the core towards the rim or
567 zoning is absent (Sevigny 1993; Bea 1996). The Y+REE contents in garnet from the Hlína
568 granite correspond well with zoning patterns observed in the BSE images (Fig. 4c) and they seem
569 to be a sensitive indicator of magmatic garnet evolution even though the self-diffusion of the
570 major divalent cations (Mn, Fe) was sufficiently rapid to eliminate any original compositional
571 zoning. Rapid growth of the garnet from undercooled melt, indicated by the sector zoning in the
572 core (Fig. 3a,b; Shelley 1992), consumed a large part of Y+HREE from the residual melt. The
573 observed Y+REE oscillatory zoning in the Hlína garnet (Fig. 3a,b) could have been produced
574 during the alternating changes in the growth and diffusion rates near the crystal-melt interface, as
575 modelled by Allègre et al. (1981) or Tsune and Toramaru (2007). Garnet/melt partition
576 coefficients for REE generally increase with increasing atomic number (Irving and Frey 1978;
577 Fujimaki et al. 1984; Green et al. 2000). Hence, the HREE are preferentially incorporated into the
578 garnet structure, residual melt is continuously impoverished during the growth of garnet I and the
579 outer part of garnet I does not reach such high Y+REE contents and the REE pattern is flatter
580 relative to the core (Fig. 7a). The outward decreasing Yb_N/Nd_N ratio during crystallization of the
581 garnet I (Fig. 7a) indicates that growth of magmatic garnet is capable of fractionating REE in the
582 melt towards the HREE-poorer pattern as shown for high-grade metamorphic garnet as well
583 (Otamendi et al. 2002). Opposite compositional Y+REE trends in garnet from peraluminous S-
584 type granites (core-rim increasing Yb_N/Nd_N ratios) reflect the growth and fractionation of
585 monazite, which depleted the liquid in LREE simultaneously with the garnet growth (Sevigny
586 1993).

587 The replacement textures observed at the outer rims of euhedral garnet (Fig. 3b,c) were
588 interpreted as products of magmatic corrosion. Higher Mn and Al, lower Ca, Y+REE content, as
589 well as higher Yb_N/Nd_N ratio and more pronounced negative Eu anomaly in the garnet II (Fig.
590 4b,7) indicate its crystallization from the more evolved melt (London 2008; Müller et al. 2012).
591 Garnet has the highest Yb_N/Nd_N ratio from the studied mineral assemblage (Fig. 5, Table 4).
592 Crystallization of other phases (with lower Yb_N/Nd_N ratio relative to garnet) during the time gap
593 between the crystallization of garnet I and garnet II increased the Yb_N/Nd_N ratio in the melt.
594 Crystallization of feldspars consuming Eu yielded more pronounced negative anomaly in the
595 more evolved melt. Consequently, garnet II shows lower ΣY+REE abundance, higher Yb_N/Nd_N
596 ratio and more negative Eu anomaly when compared to garnet I (Fig. 7). Alternatively, the lower
597 ΣY+REE and higher Yb_N/Nd_N ratio in garnet II can be attributed to the crystallization from the
598 melt relatively enriched in the volatile constituents (H_2O, B_2O_3, F) at lower temperature. Higher
599 B contents in garnet II (up to 250 ppm in garnet II and 25-67 ppm B in garnet I; Table 4) support
600 the progressive volatile enrichment. Distribution coefficients $D_{Grt/melt}$ for Y+REE in garnet
601 decrease with increasing H_2O content in the melt (Green et al. 2000) and decreasing temperature
602 in the experiments, hence hydrous magma tends to increase fractionation of HREE from LREE
603 into garnet (steeper pattern) compared to anhydrous conditions (Green et al. 2000). According to
604 Wang et al. (2003a) and Müller et al. (2012), the formation of Y-poor garnet margins
605 overgrowing the Y-rich cores indicates crystallization from volatile-enriched residual melt.

606

607 **IMPLICATIONS**

608 We documented early magmatic garnet from A-type, metaluminous to weakly peraluminous
609 granites. This garnet (<2 vol.%) is a major carrier of the Y and REE, and it incorporates 84 % Y

610 and 61 % REE of the whole-rock budget of these constituents. Detail mineral mass-balance of Y
611 and REE also revealed minor contributions of zircon and monazite. This is in contrast with the
612 majority of medium- to high-P granitic rocks where phosphates (e.g., monazite, xenotime) and
613 zircon are the major Y+REE carriers.
614 Our mass-balance calculations indiciate that a spherical layer model or a more sophisticated
615 computation for determination of the average content of major to trace elements in minerals with
616 pronounced core-rim zonation is required to obtain meaningful results. By contrast, conventional
617 arithmetic mean can provide significantly higher (in case of enriched core and depleted rim) or
618 lower (in case of depleted core and enriched rim) values.
619 Our observations indicate menzerite (and "fero-menzerite") substitution to be the main
620 incorporation mechanism of Y+REE into the Hlína garnet. It demonstrates that this substitution is
621 viable not only in higher-grade metamorphic rocks but also in low-pressure magmatic rocks.
622 Elucidation of the substitution vector introducing higher Y+REE content into the garnet is crucial
623 for proper mineral-formula calculation, including Fe^{2+}/Fe^{3+} ratio and determination of garnet
624 end-members proportions.
625 Participation of the menzerite molecule, as well as incorporation of Ca, Ti^{4+}, along with high Fe^{3+}
626 content, all promote crystallization of garnet from metaluminous to weakly peraluminous melts.
627 Crystallization of the initially Ca-rich garnet effectively eliminated Ca from the residual melt,
628 which indirectly led to an increase in ASI. This magmatic garnet is an additional example of the
629 mineral typical for peraluminous granitic rocks stabilized in weakly metaluminous granitic rock
630 by elevated contents of Ca, Fe^{3+} and Ti^{4+}. By analogy, tourmaline (schorl-dravite), another
631 characteristic mineral of strongly peraluminous granites (London 2008), is stabilized by elevated
632 contents of Ca, Fe^{3+} and Ti^{4+} in metaluminous NYF pegmatites (Novák et al. 2011; Čopjaková et
633 al. 2013) and even in alkaline pegmatite (Filip et al. 2012).

ACKNOWLEDGEMENTS

The authors are very grateful to J. S. Lackey and D. Rubatto for constructive criticism that significantly improved the manuscript and to D. London for careful handling of the manuscript. Financial support of the specific research programme of the Masaryk University (Nr.1344) is greatly acknowledged. MVG acknowledges the European Regional Development Fund project "CEITEC" - Central European Institute of Technology (CZ.1.05/1.1.00/02.0068). DD wishes to acknowledge support by the Czech Science Foundation Project Nr. P210/12/0986.

REFERENCES

Allan, B.D., and Clarke D.B. (1981) Occurrence and origin of garnet in the South Mountain batholith, Nova Scotia. Canadian Mineralogist, 19, 19-24.

Allègre, C.J., Provost, A., and Jaupart, C. (1981) Oscillatory zoning: a pathological case of crystal growth. Nature, 294, 223-228.

Anderson, J. L., Barth, A. P., Wooden, J.L., Mazdab, F. (2008) Thermometers and thermobarometers in granitic systems. Reviews in Mineralogy and Geochemistry, 69, 121-142.

Bea, F., Pereira, M.D., Corretge, L.G., Fershutcr, G.B. (1994) Differentiation of strongly peraluminous, perphosphorous granite. The Pedrobernardo pluton, central Spain. Geochimica et Cosmochimica Acta 58, 2609-2628.

Bea, E. (1996) Residence of REE, Y, Th and U in Granites and Crustal Protholiths; Implications for the Chemistry of Crustal Melts. Journal of Petrology, 37, 521-552.

Bea, F., Montero, P., Garuti, G., and Zacharini, F. (1997) Pressure dependence of rare earth element distribution in amphibolite and granulite-grade garnets. A LA-ICP-MS study. Geostandards Newsletter, 21, 253-270.

Bogoch, R., Bourne, J., Shirav, M., and Harnois, L. (1997) Petrochemistry of a Late Precambrian garnetiferous granite, pegmatite and aplite, southern Israel. Mineralogical Magazine, 61, 111-122.

Bonin, B. (2007) A-type granites and related rocks: Evolution of a concept, problems and prospects, Lithos, 97, 1–29.

Borghi, A., Compagnoni, R., Cossio, R., Giuntini, L., Massi, M., Olmi, F., Santo, A.P., and Vaggelli, G. (2006) Yttrium geothermometry applied to garnets from different metamorphic grades analyzed by EPMA and m-PIXE techniques. Microchimica Acta, 155, 105-112.

du Bray, E.A. (1988) Garnet compositions and their use as indicators of peraluminous granitoid paragenesis – southern Arabian Shield. Contributions to Mineralogy and Petrology, 100, 205-212.

Breiter, K., Čopjaková, R., and Škoda, R. (2009) The involvement of F, CO_2, and As in the alteration of Zr–Th–REE-bearing accessory minerals in the Hora Svaté Kateřiny A-type granite, Czech Republic. Canadian Mineralogist, 47, 6, 1375-1398.

Buick, I.S., Hermann, J., Williams, I.S., Gibson, R.L., and Rubatto, D. (2006) A SHRIMP U-Pb and LA-ICPMS trace element study of the petrogenesis of garnet-cordierite-orthoamphibole gneisses from the Central Zone of the Limpopo Belt, South Africa. Lithos, 88, 150-172.

Carlson, W.D. (2006) Rates of Fe, Mg, Mn, and Ca diffusion in garnet. American Mineralogist, 91, 1-11.

680 Carlson, W.D. (2012) Rates and mechanism of Y,REE, and Cr diffusion in garnet. American
681 Mineralogist, 97, 1598-1618.
682 Carmichael, I.S.E. (1991) The redox states of basic and silicic magmas: a reflection of their
683 source regions? Contributions to Mineralogy and Petrology 106, 129-141.
684 Cherniak, D.J. (1998) Rare earth element and gallium diffusion in yttrium aluminum garnet.
685 Physics and Chemistry of Minerals, 26, 156-163.
686 Černý, P., and Hawthorne, F.C. (1982) Selected peraluminous minerals. In P. Černý, P.,Ed,
687 Granitic Pegmatites in Science and Industry. Mineralogical Association of Canada, Short
688 Course Hand-book, 8, 163-186.
689 Chakraborty, S., and Ganguly, J. (1992) Cation diffusion in aluminosilicate garnets:
690 Experimental determination in spessartine-almandine diffusion couples, evaluation of
691 effective binary diffusion coeficients, and applications. Contributions to Mineralogy and
692 Petrology, 111, 74-86.
693 Čopjaková, R., Sulovský, P., and Paterson, B.A. (2005) Major and trace elements in pyrope–
694 almandine garnets as sediment provenance indicators of the Lower Carboniferous Culm
695 sediments, Drahany Uplands, Bohemian Massif. Lithos, 82, 51-70.
696 Čopjaková, R., Novák, M., and Franců, E. (2011) Formation of authigenic monazite-(Ce) to
697 monazite-(Nd) from Upper Carboniferous graywackes of the Drahany Upland: Roles of
698 the chemical composition of host rock and burial temperature. Lithos, 127, 373-385.
699 Čopjaková, R., Škoda, R., Vašinová Galiová, M., and Novák, M. (2013) Distributions of Y +
700 REE and Sc in tourmaline and their implications for the melt evolution; examples from
701 NYF pegmatites of the Třebíč Pluton, Moldanubian Zone, Czech Republic. Journal of
702 Geosciences, 58, 113-131.

703 Dahlquist, J.A. (2001) REE fractionation by accessory minerals in epidote-bearing mataluminous
704 granitoids from the Sierras Pameanas, Argentina. Mineralogical Magazine, 65, 463-475.
705 Dahlquist, J., Galindo, C., Pankhurst, R., Rapela, C.W., Alasino, P.H., Saavedra, J., and Fanning,
706 C.M. (2007) Magmatic evolution of the Penon Rosado granite: Petrogenesis of garnet-
707 bearing granitoids. Lithos, 95, 177-207.
708 Deer, W.A., Howie, R.A., and Zussman, J. (1982) Rock-Forming Minerals, Vol. 1A
709 Orthosilicates. Longman, New York. 919 pgs.
710 Diener, J.F.A., Powell, R., White, R.W., and Holland, T.J.B. (2007) A new thermodynamic
711 model for clino- and orthoamphiboles in the system Na_2O-CaO-FeO-MgO-Al_2O_3-SiO_2-
712 H_2O-O. Journal of Metamorphic Geology, 25, 631-656.
713 Diener, J.F.A., White, R.W., and Powell, R. (2008): Granulite facies metamorphism and
714 subsolidus fluid-absent reworking, Strangways Range, Arunta Block, central Australia.
715 Journal of Metamorphic Geology, 26, 603-622.
716 Dorais, M.J., and Tubrett, M. (2012) Detecting Peritectic Garnet in the Peraluminous Cardigan
717 Pluton, New Hampshire. Journal of Petrology, 53, 299-324.
718 Dudykina, A.S. (1959) Paragenetic association of trace elements in garnets of different origin.
719 Trudy Instituta Geologii Rudnych Mestorožděnij, Petrografii Mineralogii i Geochimii, 28,
720 90-110 (in Russian).
721 Eby, G.N. (1990) The A-type granitoids: A review of their occurrence and chemical
722 characteristics and speculations on their petrogenesis. Lithos, 26, 115-134.
723 Enami, M., Cong, B., Yoshida, T., and Kawabe, I. (1995) A mechanism for Na incorporation in
724 garnet. An example from garnet in orthogneiss from the Su-Lu Terrane, Eastern China.
725 American Mineralogist, 80, 475-482.

726 Erdmann, S., Jamieson, R.A., and MacDonald, M. (2009) Evaluating the origin of garnet,
727 cordierite, and biotite in granitic rocks: A case study from the South Mountain Batholith.
728 Journal of Petrology, 50, 1477-1503.
729 Filip, J., Bosi, F., Novák, M., Skogby, H., Tuček, J., Čuda, J., and Manfred, W. (2012) Iron redox
730 reactions in the tourmaline structure: High-temperature treatment of Fe^{3+}-rich schorl.
731 Geochimica et Cosmochimica Acta, 86, 239-256.
732 Finger, F., Hanžl, P., Pin, C., Quadt, A., and Steyrer, H.P. (2000) The Brunovistulicum:
733 Avalonian Precambrian at the eastern end of the Variscides. In W. Franke, R. Altherr, W.
734 Haak, O Oncken, and D Tanner, Eds., Orogenic Processes:Quantification and Modelling
735 in the Variscan Belt of Central Europe, 179, p 103-112. Geological Society London
736 Special Publication, London, UK.
737 Förster, H.J., and Rhede, D. (2006) The Be–Ta-rich granite of Seiffen (eastern
738 Erzgebirge, Germany): accessory-mineral chemistry, composition, and age of
739 a late-Variscan Li–F granite of A-type affinity. Neues Jahrbuch für Mineralogie, 182,
740 307-321.
741 Frost, B.R., and Lindsley, D. H. (1992) Equilibria among Fe-Ti oxides, pyroxenes, olivine, and
742 quartz: Part II. Application. – American Mineralogist, 77, 1004-1020.
743 Frost, C.D., Frost, B.R., Chamberlain, K.R., and Edwards, B. R. (1999) Petrogenesis of the 1.43
744 Ga Sherman Batholith, SE Wyoming, USA: a reduced, rapakivi-type anorogenic granite.
745 Journal of Petrology, 40, 1771-1802.
746 Frost, B.R., Chamberlain, K.R., and Schumacher, J.C. (2000) Sphene (titanite): phase relations
747 and role as a geochronometer. Chemical Geology, 172, 131-148.

748 Fujimaki, H., Tatsumoto, M., and Aoki, K.I. (1984) Partition coefficients of Hf, Zr, and REE
749 between phenocrysts and groundmasses. Journal of Geophysical Research, 89,
750 Supplement, B662-B672.
751 Geisler, T., Rashwan, A. A., Rahn, M. K. W., Poller, U., Zwingmann, H., Pidgeon, R. T.,
752 Schleicher, H., and Tomaschek, F. (2003) Low-temperature hydrothermal alteration of
753 natural metamict zircons from the Eastern Desert, Egypt. Mineralogical Magazine, 67,
754 485-508.
755 Geisler, T., Schaltegger, U., and Tomaschek, F. (2007) Re-equilibration of zircon in aqueous
756 fluids and melts. Elements, 3, 43-50.
757 Green, T.H., Blundy, J.D., and Adam, J. (2000) SIMS determination of trace element partition
758 coefficients between garnet, clinopyroxene and hydrous basaltic liquids at 2-7.5 GPa and
759 1080-1200°C. Lithos, 53, 165-187.
760 Grew, E.S., Marsh, J.H., and Yates M.G. (2010) Menzerite-(Y), a new species,
761 $\{(Y,REE)(Ca,Fe^{2+})_2\}[(Mg,Fe^{2+})(Fe^{3+},Al)](Si_3)O_{12}$, From a felsic granulite, Parry Sound,
762 Ontario, and a new garnet end-member, $\{Y_2Ca\}[Mg_2](Si_3)O_{12}$. Canadian Mineralogist, 48,
763 1171-1193.
764 Harrison, T.N. (1988) Magmatic garnets in the Cairngorm granite, Scotland. Mineralogical
765 Magazine, 52, 659-667.
766 Hermann, J., and Rubatto, D. (2003) Relating zircon and monazite domains to garnet growth
767 zones: age and duration of granulite facies metamorphism in the Val Malenco lower crust.
768 Journal of metamorphic Geology, 21, 833-852.
769 Hickmott, D.D., and Shimizu, N. (1990) Trace element zoning in garnet from the Kwoiek Area,
770 British Columbia: disequilibrium partitioning during garnet growth? Contribution to
771 Mineralogy and Petrology, 104, 619-630.

772 Hogan, J.P. (1996) Insights from igneous reaction space: a holistic approach to granite
773 crystallization. Transactions of the Royal Society of Edinburgh Earth Sciences, 87, 1,
774 147-158.
775 Holland, T., and Powell, R. (1991) A Compensated-Redlich-Kwong (CORK) equation for
776 volumes and fugacities of CO_2 and H_2O in the range 1 bar to 50 kbar and 100-1600 ^oC.
777 Contributions to Mineralogy and Petrology, 109, 265-273.
778 Holland, T.J.B., and Powell, R. (1998) An internally consistent thermodynamic data set for
779 phases of petrological interest. Journal of Metamorphic Geology, 16, 309-343.
780 Holland, T., and Powell, R. (2003) Activity-composition relations for phases in petrological
781 calculations: an asymmetric multicomponent formulation. Contributions to Mineralogy
782 and Petrology, 145, 492-501.
783 Holten, T., Jamtveit, B., Meakin, P., Cortini, M., Blundy, J., and Austrheim, H. (1997) Statistical
784 characteristics and origin of oscillatory zoning in crystals. American Mineralogist, 82,
785 596-606.
786 Hönig, S., Leichmann, J., and Novák, M. (2010) Unidirectional solidification textures and garnet
787 layering in Y-enriched garnet-bearing aplite-pegmatites in the Cadomian Brno Batholith,
788 Czech Republic. Journal of Geosciences, 55, 113-129.
789 Hönig, S., Leichmann, J., and Novosád, T. (2012) Garnet-bearing layered anorogenous granites
790 and pegmatites of Hlína suite inside Brunovistulicum, structures and field occurrences.
791 Geologické výzkumy Moravy a Slezska, 153-156 (in Czech).
792 Hoskin, P.W.O., and Schaltegger, U. (2003) The Composition of Zircon and Igneous and
793 Metamorphic Petrogenesis. Reviews in Mineralogy and Geochemistry, 53, 27-62.
794 Huang, R., Audétat, A. (2012) The titanium-in-quartz (TitaniQ) thermobarometer: A critical
795 examination and re-calibration. Geochimica et Cosmochimica Acta, 84, 75-89.

796 Irving, A.J., and Frey, F.A. (1978) Distribution of trace elements between garnet megacrysts and
797 host volcanic liquids of kimberlitic to rhyolitic composition. Geochimica et
798 Cosmochimica Acta, 42, 771-787.
799 Jaffe, H.W. (1951) The role of yttrium and other minor elements in the garnet group. American
800 Mineralogist, 36, 133-155.
801 Kalvoda, J., Bábek, O., Fatka, O., Leichmann, J., Melichar, R., Nehyba, S., and Špaček, P. (2008)
802 Brunovistulian Terrane (Bohemian Massif, Central Europe) from late Proterozoic to late
803 Paleozoic: an overview. International Journal of Earth Sciences, 97, 497-518.
804 Kohn, M.J. (2004) Oscillatory- and sector-zoned garnets record cyclic (?) rapid thrusting in
805 central Nepal. Geochemistry, Geophysics, Geosystems, 5, 12, Q12014, 1-9.
806 Kontak, D.J., and Corey, M. (1988) Metasomatic origin of spessartine-rich garnet in the South
807 Mountain Batholith, Nova Scotia. Canadian Mineralogist, 26, 315-334.
808 Kotková, J., and Harley, S.L. (1999) Formation and evolution of high pressure leucogranulites:
809 experimental constraints and unresolved issues. Physics and Chemistry of the Earth, Part
810 A: Solid Earth and Geodesy, 24, 299-304.
811 Kretz, R. (1983) Symbols for rock-forming minerals. American Mineralogist, 68, 277-279.¨
812 Lackey, J.S., Romero, G.A., Bouvier, A.-S., and Valley, J.W. (2012) Dynamic growth of garnet
813 in granitic magmas. Geology, 40, 171-174.
814 Lanzirotti, A. (1995) Yttrium zonning in metamorphic garnets. Geochimica et Cosmochimica
815 Acta, 59, 4105-4110.
816 Leichmann, J., and Höck, V. (2008) The Brno Batholith: an insight into the magmatic and
817 metamorphic evolution of the Cadomian Brunovistulian Unit, eastern margin of the
818 Bohemian Massif. Journal of Geosciences, 53, 218-305.

de Lima, S.E., Vannucci, R., Bottazzi, P., and Ottolini, L. (1995) Reconnaissance study of trace element zonning in garnet from the Central Structural Domain, Northeastern Brazil: an example of polymetamorphic growth. Journal of South American Earth Sciences, 8, 315-324.

London, D. (2008) Pegmatites. Canadian Mineralogist Special Publication, 10, 1-347.

London, D. (2009) The origin of primary textures in granitic pegmatites. The Canadian Mineralogist, 47, 697-724.

London, D. (2014) A petrologic assessment of internal zonation in granitic pegmatites. Lithos, 184-187, 74-104.

Loomis, T.P., Ganguly, J., and Elphick, S.C. (1985) Experimental determination of cation diffusivities in aluminosilicate garnets. II. Multicomponent simulation and tracer diffusion coeficients. Contributions to Mineralogy and Petrology, 90, 45-51.

Lyasevich, A.S, Shimanovich, N.E., Kononyuk, I.F., and Kosmyma, M.B. (1977) $Fe_5Y_3O_{12}$, $FeYO_3$: diffusion of Y. Diffusion and Defect Data, 17, 124.

Macleod, G. (1992) Zoned manganiferous garnets of magmatic origin from the Southern Uplands of Scotland. Mineralogical Magazine, 56, 115-116.

Malaspina, N., Poli, S., and Fumagalli, P. (2009) The oxidation state of metasomatized mantle wedge: insights from C-O-H-bearing garnet peridotite. Journal of Petrology, 50, 1533-1552.

Manning, D.A. (1983) Chemical variation in garnets from aplites and pegmatites, peninsular Thailand. Mineralogical Magazine, 47, 353-358.

Marsh, J.H., Grew, E.S., Gerbi, Ch.C., Yates, M.G., and Culshaw, N.G. (2012) The petrogenesis of the garnet menzerite-(Y) in granulite facies rocks of the Parry Sound Domain, Grenville Province, Ontario. Canadian Mineralogist, 50, 73-99.

Miller, C.F., and Stoddard, E.F. (1981) The role of manganese in the paragenesis of magmatic garnet: an example from the Old Woman-Puite range, California. Journal of Geology, 89, 233-246.

Müller, A., Kaersley, A., Spratt, J., and Seltmann, R. (2012) Petrogenetic implications of magmatic garnet in granitic pegmatites from southern Norway. Canadian Mineralogist, 50, 1095-1115.

Novák, M., Škoda, R., Filip, J., Macek, I., and Vaculovič, T. (2011) Compositional trends in tourmaline from intragranitic NYF pegmatites of the Třebíč Pluton, Czech Republic: an electron microprobe, Mössbauer and LA–ICP–MS study. Canadian Mineralogist, 49, 359-380.

Öhlander, B., Billström, K., and Hålenius, E. (1989) Geochemistry of the Proterozoic wolframite-bearing greisen veins and the associated granite at Rostberget, northern Sweden. Chemical Geology, 78, 135-150.

Otamendi, J.E., de la Rosa, J.D., Patino Douce, A.E., and Castro, A. (2002) Rayleigh fractionation of heavy rare earths and yttrium during metamorphic garnet growth. Geology, 30, 159-162.

Pearce, J.A., Harris, N.B.W., and Tindle, A.G. (1984) Trace element discrimination diagrams for the tectonic interpretation of the granitic rocks. Journal of Petrology, 25, 956-983.

Pyle, J.M., and Spear, F.S. (1999) Yttrium zoning in garnet: Coupling of major and accessory phases during metamorphic reactions. Geological Materials Research, 1, 1-49.

Røhr, T.S., Austrheim, H., and Erambert, M. (2007) Stress-induced redistribution of yttrium and heavy rare-earth elements (HREE) in garnet during high-grade polymetamorphism. American mineralogist, 92, 1276-1287.

Sevigny, J.H. (1993) Monazite controlled Sm/Nd fractionation in leucogranites: An Ion microprobe study of garnet phenocrysts. Geochimica Cosmochimica Acta, 57, 4095-4102.

867 Shannon, J.R., Walker, B.M., Carten, R.B., and Geraghty, E.P. (1982) Unidirectional
868 solidification textures and their significance in determining relative ages of intrusions at
869 the Henderson Mine, Colorado. Geology, 10, 293–297.
870 Sheibi, M., Esmaeily, D., Nedelec, A., Bouchez, J.L., and Kananian, A. (2010) Geochemistry and
871 petrology of garnet-bearing S-type Shir–Kuh Granite, southwest Yazd, Central Iran.
872 Island Arc, 19, 292-312.
873 Shelley, D. (1992) Igneous and Metamorphic Rocks under the Microscope. Classification,
874 Textures, Microstructures and Mineral Preferred Orientation, 211-244 p. Chapman and
875 Hall, London, U.K
876 Smeds, S.A. (1994) Zoning and fractionation trends of a peraluminous NYF granitic pegmatite
877 field at Falun, south-central Sweden. GFF, 116, 3, 175-184.
878 Spandler, C., Hermann, J., Arculus, R., and Mavrogenes, J. (2003) Redistribution of trace
879 elements during prograde metamorphism from lawsonite blueschist to eclogite facies;
880 implications for deep subduction-zone processes. Contributions to Mineralogy and
881 Petrology, 146, 205-222.
882 Spear, F.S., and Kohn, M.J. (1996) Trace element zoning in garnet as a monitor of crustal
883 melting. Geology, 24, 1099-1102.
884 Spry, P.G., Heimann, A., Messerly, J.D., and Houk, R.S. (2007) Discrimination of metamorphic
885 and metasomatic processes at the Broken Hill Pb-Zn-Ag deposit, Australia; Rare earth
886 element signature of garnet-rich rocks. Economic Geology, 102, 471-496.
887 Taylor, S.R., and McLennan, S.M. (1985) The continental crust: Its composition and evolution,
888 321p. Blackwell Scientific Publications, Palo Alto, California, USA..
889 Trumbull, R., Förster, H.J., and Rhede, D. (2010) REE-Y-Th-U-bearing accessory minerals and
890 their contribution to the lanthanide and actinide trace-element budget in an anorogenic

granite from the Erongo Complex, NW Namibia. Zeitschrift für geologische Wissenschaften, 38, 145-165.

Tsune, A., and Toramaru, A. (2007) A simple model of oscillatory zoning in magmatic plagioclase: Development of an isothermal undercooling model. American Mineralogist, 92, 1071-1079.

Vorma, A., Ojanperä, P., Hoffrén, V., Siivola, J., and Lofgren, A. (1966) On the rare earth minerals from the Pyörönmaa pegmatite in Kangasala, SW-Finland. Comptes Rendus de la Société Géologique de Finlande, 38, 241-274.

Wakita, H., Shibao, K., and Nagashima, K. (1969) Yttrian spessartine from Suishoyama, Fukushima prefecture, Japan. American Mineralogist, 54, 1678-1683.

Wang, R.C., Fontan, F., Chen X.M., Hu, H., Liu, C.S., Xu, S.J., and de Parseval, P. (2003a) Accessory minerals in the Xihuashan Y-enriched granitic complex, southern China: a record of magmatic and hydrothermal stages of evolution. Canadian Mineralogist, 41, 727-748.

Wang, R.C., Hu, H., Zhang, A., Xu, S., and Wang, D. (2003b) Yttrium zoning in garnet from the Xihuashan granitic complex and its petrologic implications. Chinese Science Bulletine, 48, 1611-1615.

Ward, C.D., McArthur, J.M., and Walsh, J.N. (1992) Rare earth element behaviour during evolution and alteration of the Dartmoor granite, SW England. Journal of Petrology, 33, 785-815.

Watson, E.B., and Harrison, T.M. (1983) Zircon saturation revisited: temperature and composition effects in a variety of crustal magma types. Earth and Planetary Science Letters, 64, 295-304.

914 Webber, K.L., Simmons, W.B., Falster, A.U., and Foord, E.E. (1999) Cooling rates and
915 crystallization dynamics of shallow level pegmatite-aplite dikes, San Diego County,
916 California. American Mineralogist, 84, 5, 708-717.
917 Whalen, J.B., Currie, K.L., and Chappell, B.W. (1987) A-type granites: geochemical
918 characteristics, discrimination and petrogenesis. Contributions to Mineralogy and
919 Petrology, 95, 407-419.
920 White, R. W., Pomroy, N. E., and Powell, R. (2005) An in-situ metatexite-diatexite transition in
921 upper amphibolite facies rocks from Broken Hill, Australia. Journal of Metamorphic
922 Geology, 23, 579-602.
923 White, R. W., Powell, R., and Holland, T. J. B. (2007) Progress relating to calculation of partial
924 melting equilibria for metapelites. Journal of Metamorphic Geology, 25, 511-527.
925 Whitworth, M.P., and Feely, M. (1994) The compositional range of magmatic Mn-garnets in Galway
926 Granite, Connemara, Ireland. Mineralogical Magazine, 58, 163-168.
927 Wones, D. R. (1989) Significance of the assemblage titanite + magnetite + quartz in granitic rocks.
928 American Mineralogist, 74, 744-749.
929 Wu, F.Y., Sun, D.Y., Jahn, B.M., and Wilde, S.A., (2004) A Jurassic garnet-bearing granitic
930 pluton from NE China showing tetrad REE patterns. Journal of Asian Earth Sciences,
931 23, 731-744.
932 Yardley, B.W.D. (1977) An empirical study of diffusion in garnet. American Mineralogist, 62,
933 793-800.
934 Zhang, J., Ma, Ch., and She, Z. (2012) An Early Cretaceous garnet-bearing metaluminous A-type
935 granite intrusion in the East Qinling Orogen, central China: Petrological, mineralogical
936 and geochemical constraints. Geoscience Frontiers, 3, 635-646.

937 Zhang, L., Zhong, Z., Zhang, H., Sun, W., and Xiang, H. (2009) The formation of foliated
938 (garnet-bearing) granites in the Tongbai-Dabie orogenic belt: partial melting of subducted
939 continental crust during exhumation. Journal of Metamorphic Geology, 27, 789-803.

940

941 Figure captions

942 Fig. 1. Up left corner – Geological map of the Brunovistulicum, AF - Alpine Front, MSFZ –
943 Moravo-Silesian Fault Zone, HKFZ – Hamburg-Krakow Fault Zone, PPFZ – Peri-Pieninian Fault
944 Zone, TESZ – Transeuropean Suture Zone ; Center – simplified regional geological map of the
945 Brno and Thaya batholiths highlighting numerous of Hlína A-type granite bodies and dykes.
946 Down right corner – detail geological map of the Hlína A-type granite. Latters refer to the
947 individual localities: A. Moravské Bránice; B. U stavení; C. Pod amfiteatrem; D. Jihlava river
948 bank. The size of the Hlína bodies is slightly enlarged compared to its real volume to better
949 display. Projection – JSTK Krovak.

950

951 Fig. 2. Photographs of the Hlína rocks: a) Contact of laminated Hlína microgranite with hosted
952 Réna I-type granite bordered by marginal UST zone. b) Garnet-bearing Hlína microgranite with
953 sharp contacts to the hosted I-type Réna granite. c) Garnet trains parallel to the lamination of the
954 Hlína laminated microgranite body. d) Detail of microgranite with garnet trains alternating with
955 unidirectional Pl, Qtz and Kfs crystals (UST).

956

957 Fig. 3. BSE images of minerals; a) euhedral garnet I with sector zoning in central part and
958 oscillatory zoning in outer part; b,c) euhedral garnet with sector and oscillatory zoning; garnet I

(brighter) is partially replaced and overgrown by garnet II (darker); d) glomerophyric garnet enclosing K-feldspar, quartz and plagioclase; e) "altered" zircon with small relics of relatively "fresh" zircon; f) euhedral garnet after LA-ICP-MS measurment with marked spherical layers used for calculation of average Y+REE content. The garnet crystals are considered as spheres that are divided in to *n-1* concentric spherical layers and the central sphere. The *n* vary from 4 to 7 and depends on the number of LA-ICP-MS analyses in the individual garnet crystal. The amounts of Y+REE in specific spherical layers and for the central sphere were calculated as a function of the volume and the Y+REE content; g) aggregate of secondary REE-bearing phases; needle-like rhabdophane-(Nd) (Ph I = phase I) predominates over U-rich secondary phase (Ph II = phase II) and clay minerals after unknown primary REE-bearing mineral; h) aggregate of secondary REE-bearing phases; U-rich secondary phase (Ph II) predominates over needle-like rhabdophane-(Nd) (Ph I) and clay minerals respecting boundary of radiation damage halo around primary accessory mineral. Primary accessory mineral is almost exclusively replaced by clay minerals.

Fig. 4. Electron microprobe results of garnet. a) Ternary plots of garnet; upper: almandine-spessartine-Ca-garnet (Ca-garnet=andradite+grossular+menzerite-(Y)); lower: grossular-andradite-menzerite-(Y). b) The profiles through euhedral garnet I replaced by garnet II. The upper plot shows variation of major and minor elements, the lower plot shows variation in the end-members. c) Correlation between zonation in BSE image and Y content in the garnet; upper: garnet I - not corroded rim; lower: garnet I partially replaced by garnet II.

Fig. 5. The REE patterns of individual minerals based on EMP data (a) and LA-ICP-MS data (b-e) and the A-type Hlína granite (f). The REE data are normalized by chondrite (Taylor and McLennan 1985). a) Zircon, rhabdophane-(Nd), U-rich phase, b) euhedral garnet, c) magnetite,

983 d) muscovite and epidote, e) plagioclase and K-feldspar. Arithmetic mean for Y+REE contents or
984 compositional range for individual minerals are ploted depending on the REE data heterogeneity.

985

986 Fig. 6. Intrusive setting of the Hlína A-type granite shown in various tectonic discrimination plots
987 after Pearce et al. (1984), Whalen et al. (1987) and Eby (1990); a) (Y+Nb) vs. Rb plot; b) Y vs.
988 Nb plot; c) (10000*Ga/Al) vs. Zr plot; d) ternary 3*Ga-Nb-Y diagram. Abbreviations: WPG -
989 Within Plate Granites; ORG - Ocean Ridge Granites, VAG - Volcanic Arc Granites, syn-COLG -
990 Syn Collisional Granites; A1 - A-type granite field associated with hotspots, mantle plumes
991 and/or continental rift zones; A2 - A-type granite field with post-collision, post-orogenic and
992 anorogenic affinity.

993

994 Fig. 7. The 2D plots for Y+REE in garnet with simplified garnet crystallization scheme;
995 Yb_N/Sm_N ratio vs. Y+REE content for a) all garnet analysis and b) average values for garnet
996 grains; Yb_N/Sm_N ratio vs. Eu/Eu* for c) all garnet analysis and d) average values for garnet
997 grains. The dotted lines in b) and d) join average values of garnet I and garnet II within each
998 garnet grain.

999

1000 Fig. 8. a) The chondrite normalized REE+Y pattern of the whole rock (WR - blue symbols;
1001 average of the MB1-1, MB1-52 and MB1-55 samples) and patterns calculated according to
1002 models A and B. Dashed red line and open symbols - model A - calculated from primary mineral
1003 mass fractions and their average Y+REE content (Grt, Zrn, Ms, Mag, Qtz, Pl, Kfs and Ep; used
1004 abbreviations after Kretz 1983). Solid red symbols and line - model B – including REE-bearing
1005 secondary phases in addition to the primary minerals involved in the model A.

b) Contribution of the rock-forming minerals (Grt, Zrn, Ms, Mag, Qtz, Pl, Kfs, Ep and secondary REE-bearing phases) to the budget of individual REE+Y. The height of the bar is normalized to 100 % (scale on the left side Y axis). For the comparison, chondrite normalized REE+Y content is drawn as the gray underlying field (scale on the right side Y axis).

Fig. 9. The temperature-log oxygen fugacity diagram at P = 1 kbar and H_2O saturation illustrating the location of common fO_2 buffers as well as equilibria relevant to the garnet- and magnetite-bearing granites in the present study. The zircon saturation temperature (734 ± 14 ^oC) constrains the maximum temperature limit for closed-system crystallization. At these conditions, composition of garnet I and the absence of fayalite restrict the plaussible redox conditions up to 1.2 log units above the QFM buffer. Intercepts of multiple equilibria between magnetite, garnet, quartz and plagioclase at 657-663 ^oC (for garnet I rim and garnet II overwgrowths) are interpreted as being close to the final solidification temperature. The course of the skiagite-magnetite-quartz equilibrium is nearly parallel to the QFM buffer, therefore, the crystallization could have commenced metastably below ~730 ^oC and/or isothermally near 660 ^oC. Mineral and end-member abbreviations: an – anorthite, andr – andradite, anth – anthophyllite, fa – fayalite, gr – grossular, hm – hematite, mt – magnetite, q – quartz, ski – skiagite.

Fig. 10. Binary plots showing major substitution trends involving Y in euhedral garnet. Full circles - garnet I, open circles - garnet II.

Table caption

Table 1. Electron microprobe analysis of the euhedral and glomerophyric garnet and calculation of proportional end-members content (in mol. %).

Table 2. Electron microprobe analysis of fresh and altered zircon (Zrn) and rhabdophane-(Nd) (Rhb). Mineral formulae of both phases were calculated using normalization on 4 anions.

Table 3. Whole rock analyses of the A-type Hlína granite.

Table 4. Trace element analyses (LA-ICP-MS data) of rock forming minerals from the Hlína granite: Grt I-primary garnet, Grt II-secondary garnet, (c-core, r-rim), Ms-muscovite, Mag-magnetite, Pl-plagioclase, Kfs-K-feldspar, Qtz-quartz (average of 15 analyses), Ep-epidote (average of 7 analyses) All data are in wt. ppm. na-not analysed.

Table 5. Mineral fractions in the Hlína granite calculated expressed in vol. % and proportional fraction of Y, ∑REE, ∑LREE and ∑HREE in individual minerals.

Table 6. Average Y+REE content calculated from MB1-1, MB1-52 and MB1-55 samples and calculated proportional Y and REE content of individual minerals. LREE phs-secondary LREE-bearing phases, other abbreviations are the same as in table 4.

	euhedral garnet							glomerophyric garnet	
	Grt I core	Grt I core	Grt I core	Grt I rim	Grt I rim	Grt II	Grt II	Grt I core	Grt I rim
SiO_2	35.73	35.99	35.81	36.43	36.35	36.76	36.52	36.17	36.94
TiO_2	0.40	0.43	0.44	0.20	0.20	0.04	0.04	0.52	0.30
Al_2O_3	16.78	16.93	16.96	18.25	18.45	20.22	19.85	16.70	18.40
Fe_2O_3	3.40	2.70	3.40	1.81	1.62	0.00	1.42	3.87	2.99
Y_2O_3	1.83	1.66	1.67	0.91	0.95	0.34	0.36	1.59	0.54
Er_2O_3	0.22	0.24	0.23	0.17	0.10	0.08	0.06	0.45	0.08
Yb_2O_3	0.50	0.51	0.51	0.22	0.22	0.13	0.13	0.30	0.04
MgO	0.38	0.34	0.37	0.36	0.41	0.35	0.36	0.38	0.33
CaO	7.64	7.33	7.40	6.02	5.69	4.04	4.25	8.05	6.64
FeO	13.40	13.80	13.17	16.31	16.58	18.64	17.28	13.17	15.34
MnO	18.65	18.87	18.92	18.38	18.35	18.88	19.85	18.90	19.48
Na_2O	0.07	0.11	0.16	0.10	0.10	0.05	0.05	0.09	0.06
Σ oxides	99.00	98.91	99.04	99.16	99.01	99.53	100.17	100.19	101.14
Si^{4+}	2.995	3.015	2.996	3.022	3.017	3.018	2.990	2.995	3.001
Ti^{4+}	0.025	0.027	0.028	0.012	0.012	0.002	0.002	0.032	0.018
Al^{3+}	1.657	1.671	1.672	1.784	1.805	1.956	1.915	1.630	1.762
Fe^{3+}	0.214	0.170	0.214	0.113	0.101	0.000	0.088	0.241	0.183
Y^{3+}	0.082	0.074	0.074	0.040	0.042	0.015	0.016	0.070	0.023
Er^{3+}	0.006	0.006	0.006	0.004	0.003	0.002	0.002	0.011	0.002
Yb^{3+}	0.013	0.013	0.013	0.006	0.006	0.003	0.003	0.008	0.001
Mg^{2+}	0.047	0.042	0.046	0.045	0.051	0.043	0.044	0.047	0.040
Ca^{2+}	0.686	0.658	0.663	0.535	0.506	0.355	0.373	0.714	0.578
Fe^{2+}	0.940	0.967	0.921	1.131	1.151	1.280	1.183	0.912	1.042
Mn^{2+}	1.324	1.339	1.341	1.291	1.290	1.313	1.376	1.325	1.340
Na^{+}	0.011	0.018	0.026	0.016	0.016	0.008	0.008	0.014	0.009
Σ cations	8.000	8.000	8.000	7.999	8.000	7.995	8.000	8.000	8.000
O	12.000	12.000	12.000	12.000	12.000	12.000	12.000	12.000	12.000

pyrope	0.0	0.0	0.0	0.4	0.5	1.0	1.0	0.0	0.8
spessartine	44.1	44.6	44.7	43.0	43.0	43.8	45.9	44.2	44.7
Na-Y garnet	0.7	1.2	1.7	1.1	1.1	0.5	0.5	0.9	0.6
morimotoite	2.5	2.7	2.8	1.2	1.2	0.2	0.2	3.2	1.8
menzerite	4.5	3.8	3.4	1.7	1.8	0.6	0.7	3.8	0.9
almandine	29.1	30.2	29.1	37.3	38.0	42.6	39.4	28.4	34.1
andradite	10.7	8.5	10.7	5.7	5.1	0.0	4.4	12.1	9.2
grossular	8.2	9.5	7.5	10.4	10.0	11.4	7.6	7.3	8.0

	"fresh" Zrn	"altered" Zrn	Rhb	Rhb		"fresh" Zrn	"altered" Zrn	Rhb	Rhb
SO_3	0.02	0.18	0.29	0.00	S^{6+}	0.001	0.005	0.009	0.000
P_2O_5	bdl	6.77	20.76	19.49	P^{5+}	0.000	0.208	0.703	0.695
Nb_2O_5	bdl	1.00	bdl	bdl	Si^{4+}	0.951	0.678	0.307	0.294
SiO_2	28.53	18.71	7.68	6.98	*subtotal*	*0.952*	*0.891*	*1.019*	*0.989*
TiO_2	na	na	bdl	0.05	Nb^{5+}	0.000	0.016	0.000	0.000
ZrO_2	57.54	41.04	1.48	0.39	Ti^{4+}	na	na	0.000	0.001
HfO_2	7.82	1.77	bdl	bdl	Zr^{4+}	0.935	0.725	0.029	0.008
ThO_2	0.30	1.28	7.53	24.49	Hf^{4+}	0.074	0.018	0.000	0.000
UO_2	1.53	0.63	0.25	0.96	Th^{4+}	0.002	0.011	0.069	0.235
AlO_3	0.08	3.76	na	na	U^{4+}	0.011	0.005	0.002	0.009
Sc_2O_3	0.02	0.07	na	na	Al^{3+}	0.003	0.161	na	na
As_2O_3	0.12	0.08	bdl	bdl	Sc^{3+}	0.001	0.002	na	na
Y_2O_3	0.62	5.88	3.36	5.44	As^{3+}	0.002	0.002	0.000	0.000
La_2O_3	bdl	0.04	6.86	4.88	Y^{3+}	0.011	0.113	0.071	0.122
Ce_2O_3	bdl	0.28	11.18	1.97	La^{3+}	0.000	0.001	0.101	0.076
Pr_2O_3	bdl	0.05	3.04	1.69	Ce^{3+}	0.000	0.004	0.164	0.030
Nd_2O_3	bdl	0.21	12.93	8.24	Pr^{3+}	0.000	0.001	0.044	0.026
Sm_2O_3	0.01	0.23	5.04	3.12	Nd^{3+}	0.000	0.003	0.185	0.124
Eu_2O_3	bdl	bdl	bdl	bdl	Sm^{3+}	0.000	0.003	0.069	0.045
Gd_2O_3	0.02	0.52	3.67	2.98	Eu^{3+}	0.000	0.000	0.000	0.000
Tb_2O_3	bdl	0.09	na	na	Gd^{3+}	0.000	0.006	0.049	0.042
Dy_2O_3	0.04	0.92	1.22	1.27	Tb^{3+}	0.000	0.001	na	na
Ho_2O_3	0.02	0.17	na	na	Dy^{3+}	0.000	0.011	0.016	0.017
Er_2O_3	0.11	0.54	0.33	0.32	Ho^{3+}	0.000	0.002	na	na
Yb_2O_3	0.17	0.61	na	na	Er^{3+}	0.001	0.006	0.004	0.004
Lu_2O_3	0.35	0.24	na	na	Yb^{3+}	0.002	0.007	na	na
CaO	0.09	0.30	5.54	7.62	Lu^{3+}	0.004	0.003	na	na
SrO	na	na	0.33	0.25	Ca^{2+}	0.003	0.012	0.237	0.344
FeO	0.33	1.08	2.06	1.92	Sr^{2+}	na	na	0.008	0.006

PbO	0.11	0.13	0.49	0.56	Fe^{2+}	0.009	0.033	0.069	0.067
Na_2O	na	na	0.21	0.08	Pb^{2+}	0.001	0.001	0.005	0.006
F	bdl	0.37	0.31	0.18	Na^{+}	na	na	0.017	0.007
O=F		-0.16	-0.12	-0.08	*subtotal*	*1.059*	*1.147*	*1.139*	*1.169*
∑ oxides	97.83	86.79	94.41	92.77	∑ cations	2.013	2.035	2.158	2.158
					F^{-}	0.000	0.042	0.039	0.024
					O^{2-}	4.000	3.958	3.961	3.976
					∑ anions	4.000	4.000	4.000	4.000

Locality	A	A	A	B	B	C	D
Sample	MB1-1	MB1-52	MB1-55	J/21b	J/21c	J Re	J Iv
SiO_2	75.72	74.90	74.61	75.79	75.86	74.92	75.46
TiO_2	0.03	0.03	0.03	0.03	0.04	0.04	0.04
Al_2O_3	13.60	14.90	13.83	13.64	16.60	13.48	13.27
$Fe_2O_3^{tot}$	0.62	0.71	0.93	0.90	0.71	0.79	0.84
MnO	0.12	0.13	0.32	0.10	0.09	0.04	0.90
MgO	0.02	0.02	0.03	0.03	0.03	0.03	0.02
CaO	0.94	1.11	1.10	0.96	1.20	1.16	0.61
Na_2O	4.30	4.21	3.82	3.85	3.85	3.93	4.18
K_2O	4.69	4.61	4.94	4.21	4.29	4.15	4.11
P_2O_5	0.02	0.04	0.05	0.02	0.01	0.01	0.01
LOI	0.4	0.3	0.5	0.3	0.3	0.7	0.5
∑ oxides	100.25	100.22	100.27	99.71	99.8	99.25	99.13
Ba	17	4	31	18	14	17	46
Cs	3.9	3.1	2.9	na	na	na	na
Hf	4.5	6.3	6.8	na	na	na	na
Rb	182	180	170	174	156	174	311
Sr	13	13	22	22	21	30	16
Ta	4	2	2.1	na	na	na	na
Zr	66	101	107	79	74	76	72
Y	45	64	116	56	47	23	14
Ga	18	19	18	24	21	20	19
U	7	6	8	12	17	7	16
Th	13	15	18	12	17	7	16
Nb	28	11	13	51	46	19	23
La	2.30	2.30	3.00	2.00	3.00	3.50	1.90
Ce	5.70	5.90	8.50	5.00	6.10	6.70	5.20
Pr	0.75	0.92	1.25	0.87	1.16	1.25	0.53
Nd	3.40	4.90	5.90	4.30	5.00	5.10	2.40
Sm	1.85	2.15	2.93	2.20	2.80	2.30	1.40
Eu	0.14	0.17	0.18	0.21	0.19	0.27	0.10
Gd	2.91	3.58	5.62	3.44	3.26	2.34	2.97
Tb	0.76	0.94	1.66	0.74	0.71	0.44	0.79
Dy	5.79	7.56	12.97	6.51	5.53	2.94	6.48
Ho	1.35	1.90	3.14	1.64	1.45	0.81	1.80
Er	4.91	7.34	11.32	6.30	5.80	2.58	6.26

Tm	1.20	1.47	2.24	1.23	1.20	0.46	1.90
Yb	7.30	10.40	15.90	9.18	7.80	4.43	10.30
Lu	1.25	1.95	2.75	1.75	1.44	0.76	1.74
ASI	0.98	1.07	1.01	1.08	1.03	1.03	1.07
K/Rb	214	212	241	201	228	198	110
K/Ba	2304	1034	1327	1941	2544	2026	742
mg#	5	5	5	6	7	6	4
La_N/Yb_N	0.21	0.15	0.13	0.15	0.29	0.53	0.13
Eu/Eu*	0.18	0.19	0.14	0.23	0.19	0.36	0.15

	garnet grain 8 Grt I-c	garnet grain 8 Grt I-r	garnet grain 5 Grt I-c	garnet grain 5 Grt I-r	garnet grain 5 Grt II	garnet grain 10 Grt I-c	garnet grain 10 Grt I-r	garnet grain 10 Grt II	garnet grain 9 Grt I-c	garnet grain 9 Grt I-r	garnet grain 9 Grt II
B	bdl	67	na	na	na	66	25	93	47	bdl	250
Ti	2513	1165	na	na	na	1625	1106	151	1690	809	198
Zr	25.7	4.8	22.7	4.9	8.5	4.6	2.7	0.5	4.9	3.4	0.6
Nb	6.7	0.7	na	na	na	2.0	0.8	bdl	2.8	1.0	0.1
Ta	1.9	1.0	na	na	na	0.5	0.4	bdl	1.1	0.5	0.1
Nb/Ta	3.55	0.72				3.64	1.91		2.65	2.19	0.84
Y	15534	3756	14447	6780	3151	10090	5951	2973	11069	9438	4704
La	0.08	0.02	0.02	0.03	0.01	0.01	bdl	bdl	bdl	bdl	0.01
Ce	0.31	0.08	0.24	0.48	0.10	0.08	0.04	0.01	0.05	bdl	bdl
Pr	0.18	0.06	0.05	0.12	0.03	0.07	0.05	0.00	0.06	0.04	0.01
Nd	3.67	1.55	3.27	2.71	0.65	2.66	1.89	0.24	2.98	2.17	0.43
Sm	35.06	17.94	23.22	26.93	4.74	26.12	18.67	3.09	28.67	23.02	5.62
Eu	1.48	0.64	0.88	0.84	0.09	1.09	0.58	0.06	1.24	0.88	0.20
Gd	305.4	153.8	191.2	197.9	43.2	228.2	176.5	47.0	276.4	222.5	63.4
Tb	131.7	57.7	89.2	76.0	21.0	106.4	72.5	23.2	123.7	98.5	30.7
Dy	1738	532	1134	683	250	1125	673	302	1481	1084	378
Ho	548	112	391	157	93	327	168	120	488	372	160
Er	2043	291	1636	444	440	1101	532	578	1927	1345	685
Tm	399	72	366	72	103	205	107	141	406	268	183
Yb	4157	720	3288	528	1058	1808	943	1388	3526	2466	1811
Lu	629	91	613	78	211	271	145	260	566	391	346
ΣREE	9992	2049	7735	2267	2224	5202	2838	2863	8829	6273	3663
Yb_N/Sm_N	105	36	126	17	198	61	45	398	109	95	285
Eu/Eu*	0.044	0.038	0.041	0.035	0.020	0.044	0.031	0.016	0.043	0.038	0.032

	Ms	Ms		Mag	Mag	Pl	Pl	Kfs	Kfs	Qtz avg	Ep avg
B	7343	2829	Mn	6413	1153						
Ti	754	1190	Ti	19209	3690						
Zr	17.2	49.5	Zr	373	477	0.81	1.51	0.78	0.52		
Y	4.07	38.41	Y	58.7	73.5	1.14	0.40	0.12	1.08	1.72	10.25
La	2.03	7.71	La	17.5	13.1	0.56	0.40	0.06	0.15	0.32	13.07
Ce	11.77	24.76	Ce	23.6	19.5	0.54	0.84	0.08	0.31	0.73	10.01
Pr	0.34	1.47	Pr	4.3	3.8	0.11	0.12	0.04	0.03	0.13	1.82
Nd	1.19	6.01	Nd	18.9	16.9	0.30	0.34	bdl	0.15	0.87	5.80
Sm	0.30	2.22	Sm	8.7	8.9	0.10	0.05	bdl	0.08	0.22	1.80
Eu	0.12	0.41	Eu	0.34	0.38	0.23	0.32	0.23	0.22	0.01	0.00

Gd	1.41	2.53	Gd	9.7	12.3	0.13	0.16	0.21	0.12	0.17	na
Tb	0.32	0.76	Tb	1.75	2.45	0.04	0.02	0.03	0.12	0.05	na
Dy	1.57	4.14	Dy	11.5	16.4	0.15	0.11	bdl	0.18	0.09	na
Ho	0.33	0.79	Ho	2.35	3.32	0.02	bdl	bdl	0.09	0.26	na
Er	1.16	2.25	Er	6.15	9.67	0.02	0.05	0.05	0.11	0.25	na
Tm	0.19	0.33	Tm	0.85	1.38	bdl	bdl	bdl	bdl	0.12	na
Yb	1.15	2.67	Yb	5.95	10.47	0.03	bdl	bdl	0.11	0.13	na
Lu	0.21	0.56	Lu	0.91	1.79	bdl	bdl	bdl	bdl	0.18	na
ΣREE	22	57	ΣREE	112	120	3.29	2.82	0.81	2.48	5.26	42.75
La_N/Yb_N	1.14	1.87	La_N/Yb_N	1.90	0.81						
Eu/Eu*	0.56	0.53	Eu/Eu*	0.11	0.11	6.6	10.5		6.9		
Ce/Ce*	3.14	1.64	Ce/Ce*	0.61	0.62						

	mineral fraction in the WR [%]	proportional fraction in individual minerals			
		Y [%]	REE [%]	La-Gd [%]	Tb-Lu [%]
Garnet	0.9	83.6	61.0	8.8	85.8
Zircon	0.026	12.5	10.7	10.8	10.6
Muscovite	3.8	0.8	1.6	3.8	0.5
Magnetite	0.9	0.7	1.7	3.5	0.8
Plagioclase	36.7	0.3	1.8	4.9	0.4
K-feldspar	26.8	0.1	0.5	1.2	0.1
Quartz	30.8	0.8	1.8	3.9	0.8
Epidote	0.120	0.0	0.1	0.3	n.d.
LREE phs	0.003	1.1	20.9	62.8	1.0

LREE phs = secondary REE-bearing phases

	average Y+REE in the WR [ppm]	proportional fraction of Y and REE of individual minerals [%]									
		Grt	**Zrn**	**Ms**	**Mag**	**Pl**	**Kfs**	**Qtz**	**Ep**	**LREE phs**	**Total**
La	7.45	0.0	2.9	4.4	5.7	8.1	1.2	4.4	0.9	72.4	100.0
Ce	7.36	0.0	7.0	6.5	2.7	4.4	0.8	3.4	0.2	75.0	100.0
Pr	8.04	0.1	4.3	2.9	3.8	4.1	0.9	4.4	0.3	79.2	100.0
Nd	7.40	0.4	7.4	2.3	3.7	4.8	1.0	6.5	0.2	73.8	100.0
Sm	11.85	8.1	18.3	1.9	3.8	3.1	1.2	3.4	0.1	60.1	100.0
Eu	2.24	3.8	0.0	3.1	2.1	53.4	35.3	2.3	0.0	0.0	100.0
Gd	15.53	42.7	23.6	1.3	2.9	2.4	0.6	1.5	0.0	25.0	100.0
Tb	23.83	73.6	19.2	1.3	2.1	1.5	0.8	1.6	0.0	0.0	100.0
Dy	29.24	79.2	14.2	0.8	1.4	0.8	0.1	0.3	0.0	3.3	100.0
Ho	27.31	82.8	11.9	0.5	0.9	0.5	0.3	3.1	0.0	0.0	100.0
Er	39.28	85.8	10.9	0.5	0.7	0.2	0.1	0.9	0.0	0.9	100.0
Tm	49.27	87.2	9.5	0.4	0.6	0.2	0.1	2.0	0.0	0.0	100.0
Yb	50.94	90.6	8.0	0.3	0.6	0.2	0.0	0.3	0.0	0.0	100.0
Lu	59.31	87.8	9.1	0.3	0.5	0.1	0.0	2.2	0.0	0.0	100.0
Y	44.27	83.6	12.5	0.8	0.7	0.3	0.1	0.8	0.0	1.1	100.0

LREE phs = secondary REE-bearing phases

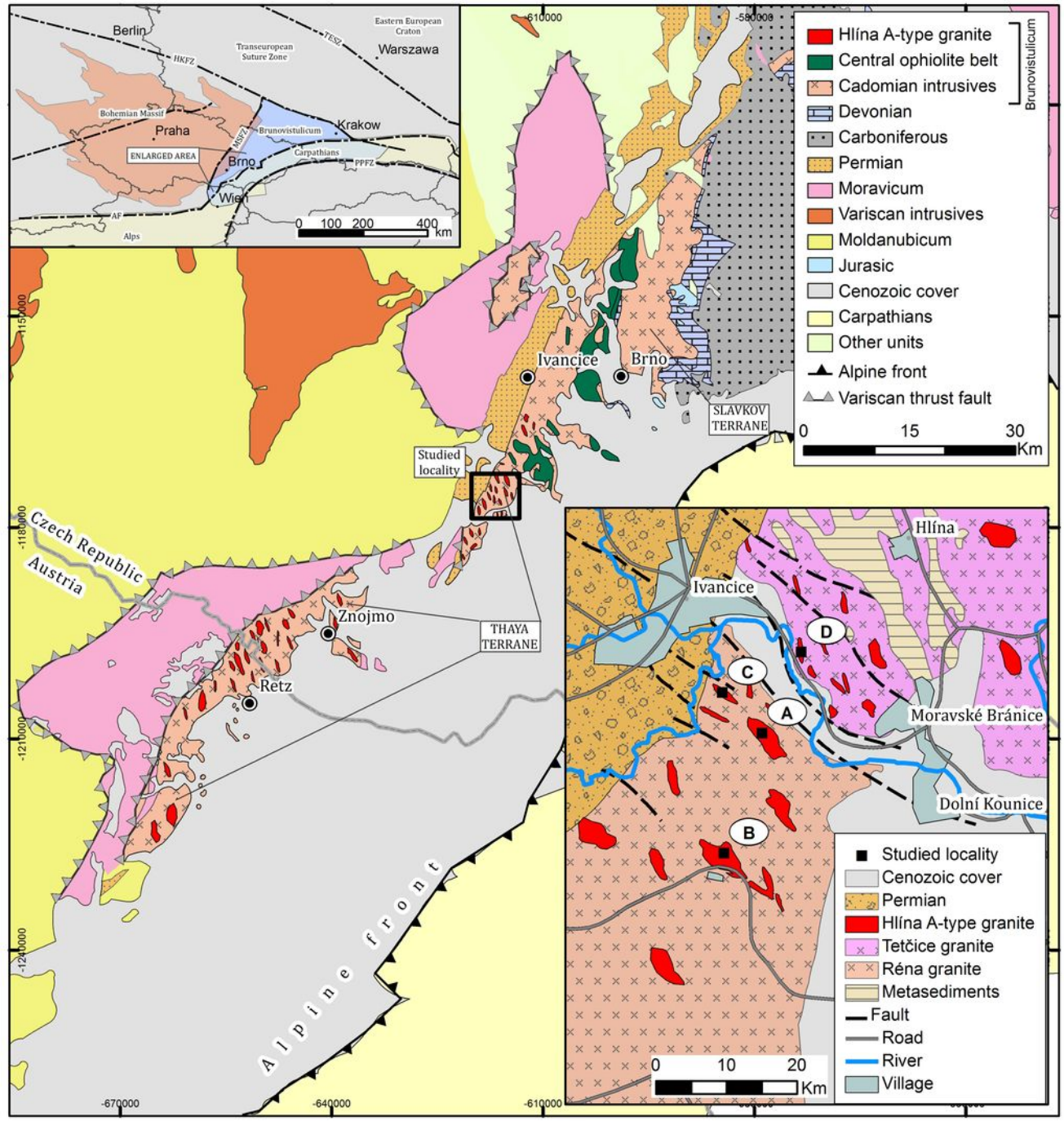
Berlin
Eastern European Craton
Transeuropean Suture Zone
TESZ
HKFZ
Warszawa
Bohemian Massif
Praha
MSFZ
Brunovistulicum
Krakow
ENLARGED AREA
Brno
Carpathians
PPFZ
Wien
AF
Alps
0 100 200 400 km
-610000
-590000
-1150000
-1180000
-1210000
-1240000
-670000
-640000
-610000
Hlína A-type granite
Central ophiolite belt
Cadomian intrusives
Devonian
Carboniferous
Permian
Moravicum
Variscan intrusives
Moldanubicum
Jurasic
Cenozoic cover
Carpathians
Other units
Alpine front
Variscan thrust fault
Brunovistulicum
0 15 30 Km
Ivancice
Brno
SLAVKOV TERRANE
Studied locality
Czech Republic
Austria
Znojmo
Retz
THAYA TERRANE
Alpine front
Hlína
Ivancice
D
C
A
B
Moravské Bránice
Dolní Kounice
Studied locality
Cenozoic cover
Permian
Hlína A-type granite
Tetčice granite
Réna granite
Metasediments
Fault
Road
River
Village
0 10 20 Km

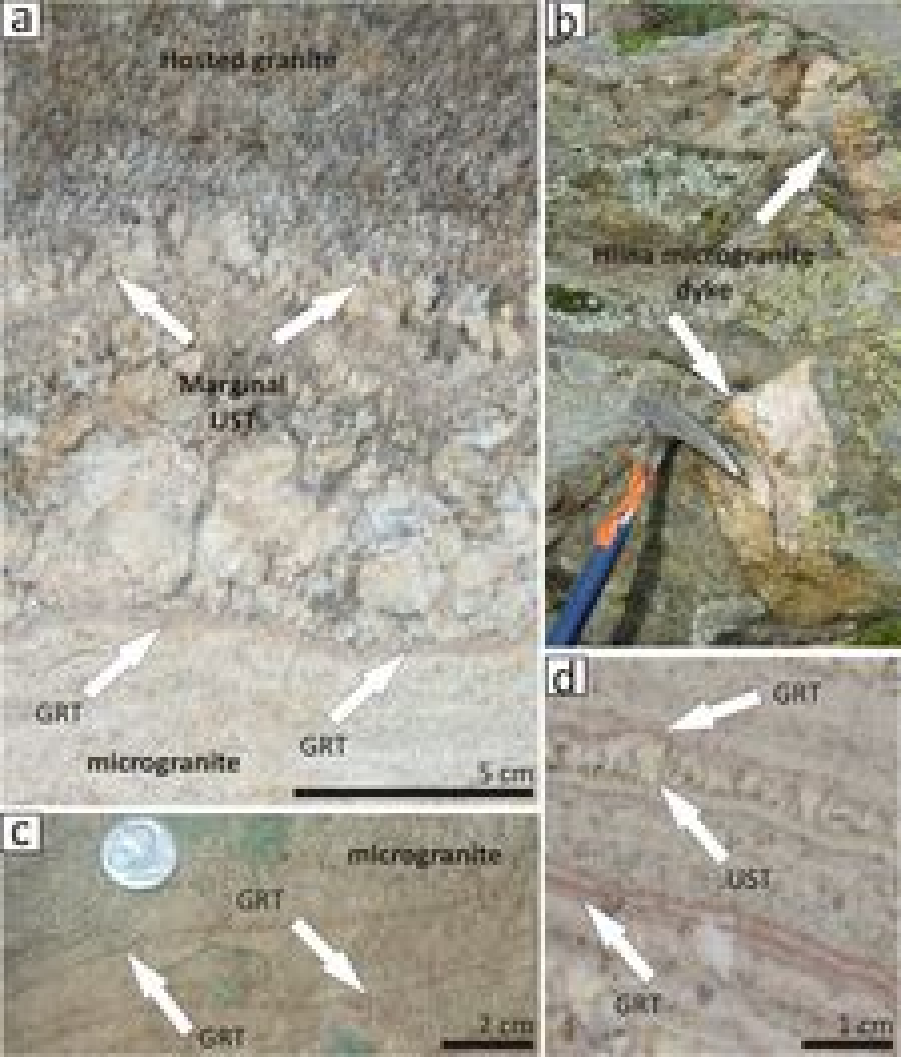
a
Hosted granite
Marginal
UST
GRT
GRT
microgranite
5 cm
b
Hilea microgranite
dyke
c
microgranite
GRT
GRT
2 cm
d
GRT
UST
GRT
2 cm

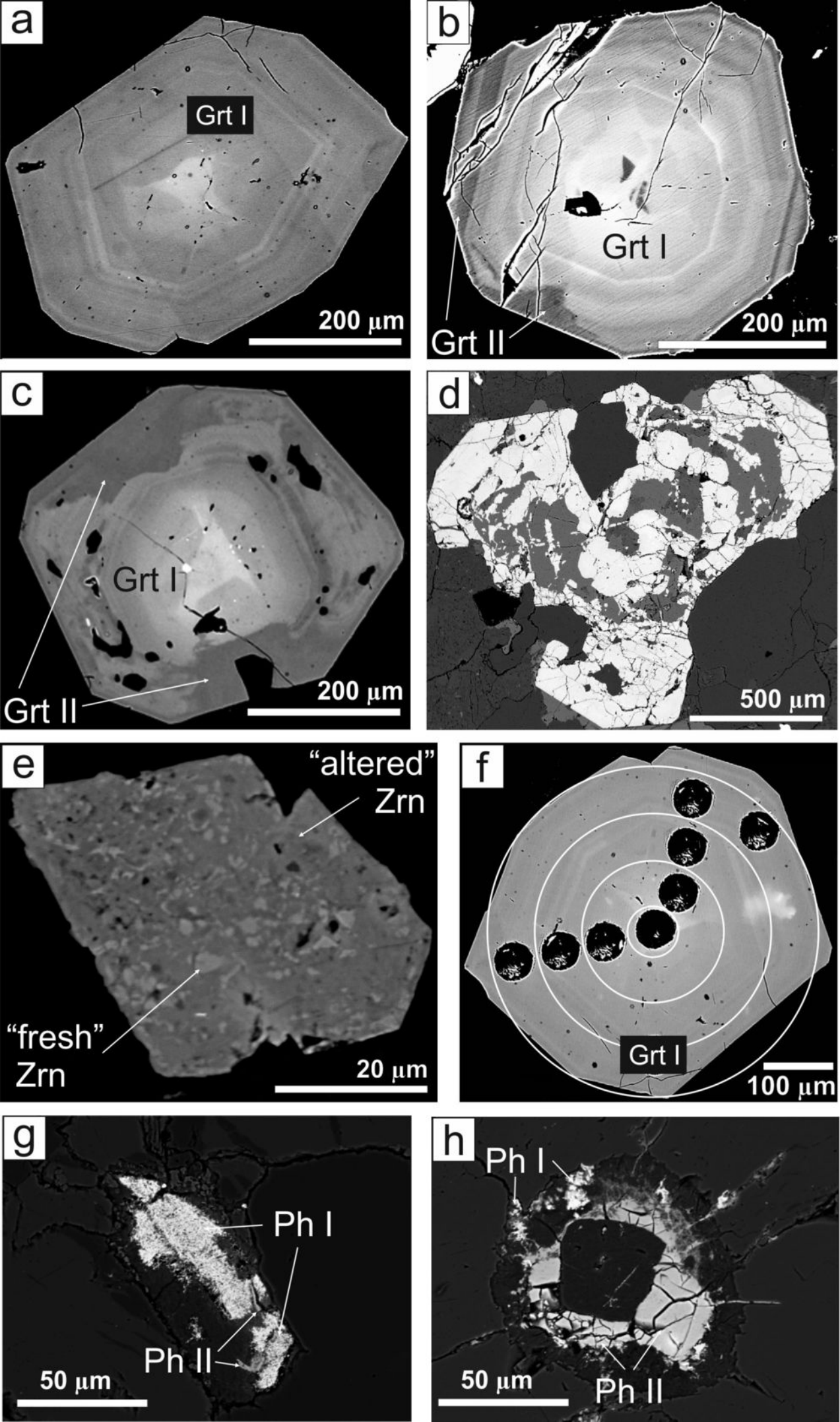
a
Grt I
200 μm
b
Grt I
Grt II
200 μm
c
Grt I
Grt II
200 μm
d
500 μm
e
"altered"
Zrn
"fresh"
Zrn
20 μm
f
Grt I
100 μm
g
Ph I
Ph II
50 μm
h
Ph I
50 μm
Ph II

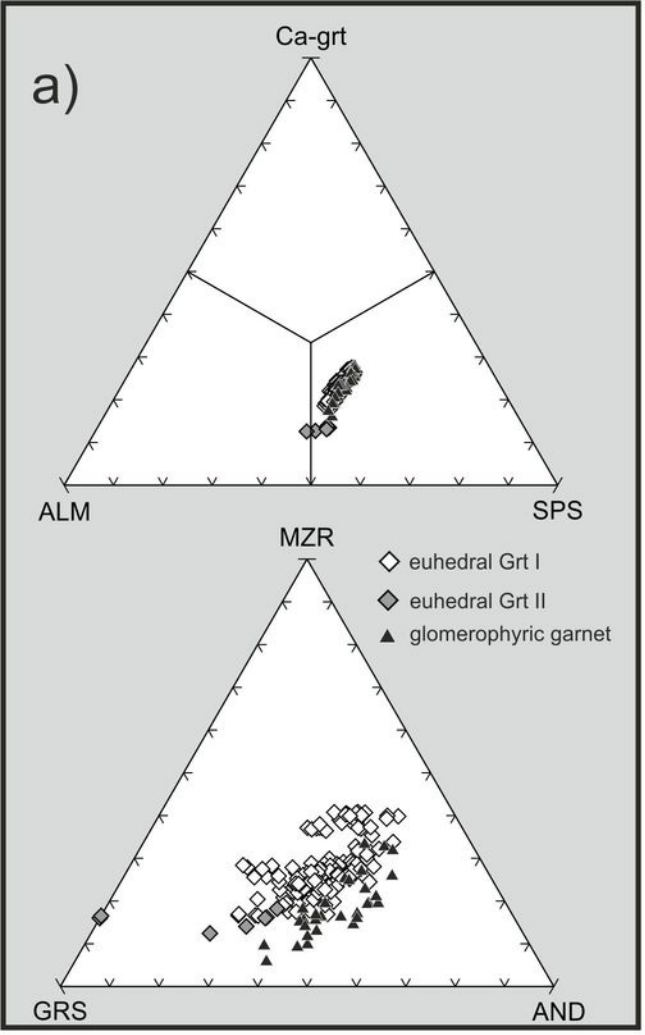
a)
Ca-grt
ALM
SPS
MZR
GRS
AND
euhedral Grt I
euhedral Grt II
glomerophyric garnet

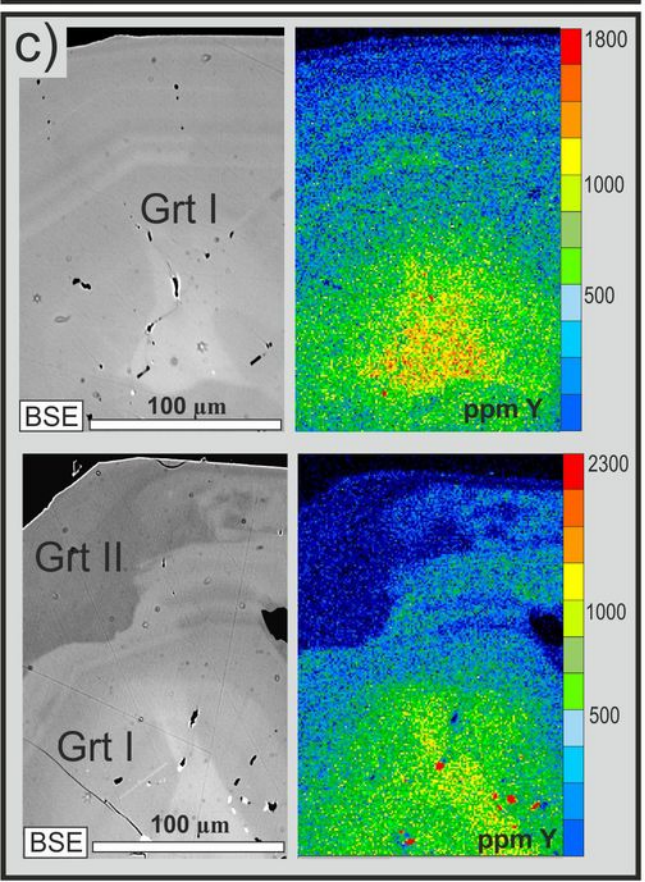
c)
Grt I
BSE
100 µm
ppm Y
1800
1000
500
Grt II
Grt I
BSE
100 µm
ppm Y
2300
1000
500

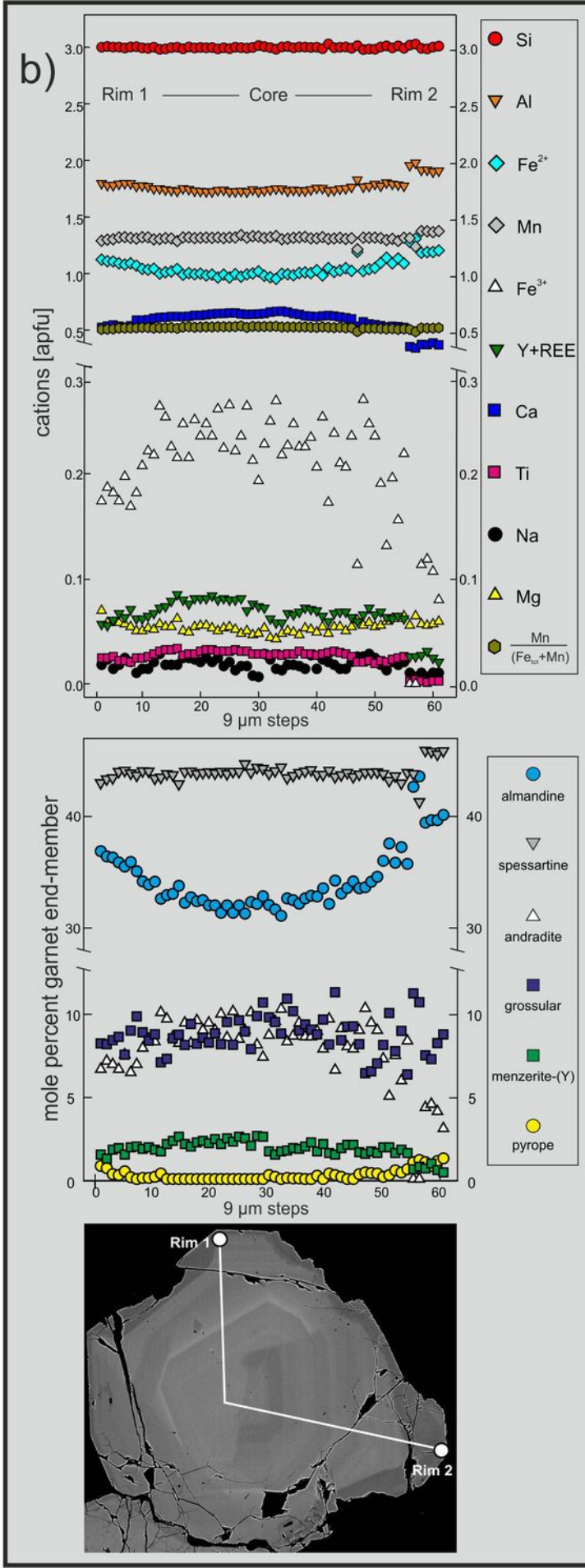
b)
Rim 1
Core
Rim 2
cations [apfu]
9 µm steps
Si
Al
Fe2+
Mn
Fe3+
Y+REE
Ca
Ti
Na
Mg
Mn/(Fetot+Mn)
mole percent garnet end-member
almandine
spessartine
andradite
grossular
menzerite-(Y)
pyrope
Rim 1
Rim 2

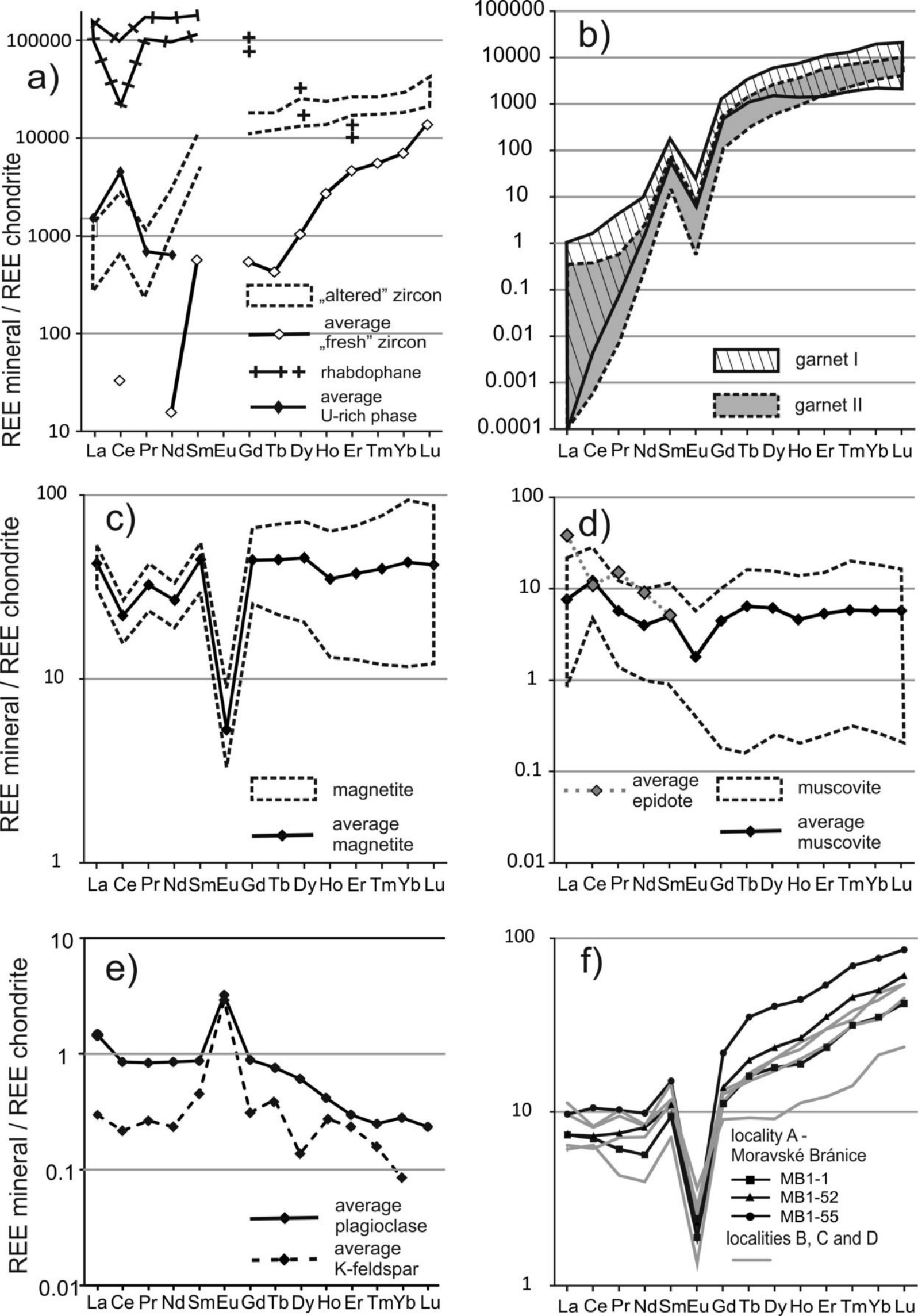
a)
b)
c)
d)
e)
f)
REE mineral / REE chondrite
La Ce Pr Nd Sm Eu Gd Tb Dy Ho Er Tm Yb Lu
„altered" zircon
average „fresh" zircon
rhabdophane
average U-rich phase
garnet I
garnet II
magnetite
average magnetite
average epidote
muscovite
average muscovite
average plagioclase
average K-feldspar
locality A - Moravské Bránice
MB1-1
MB1-52
MB1-55
localities B, C and D

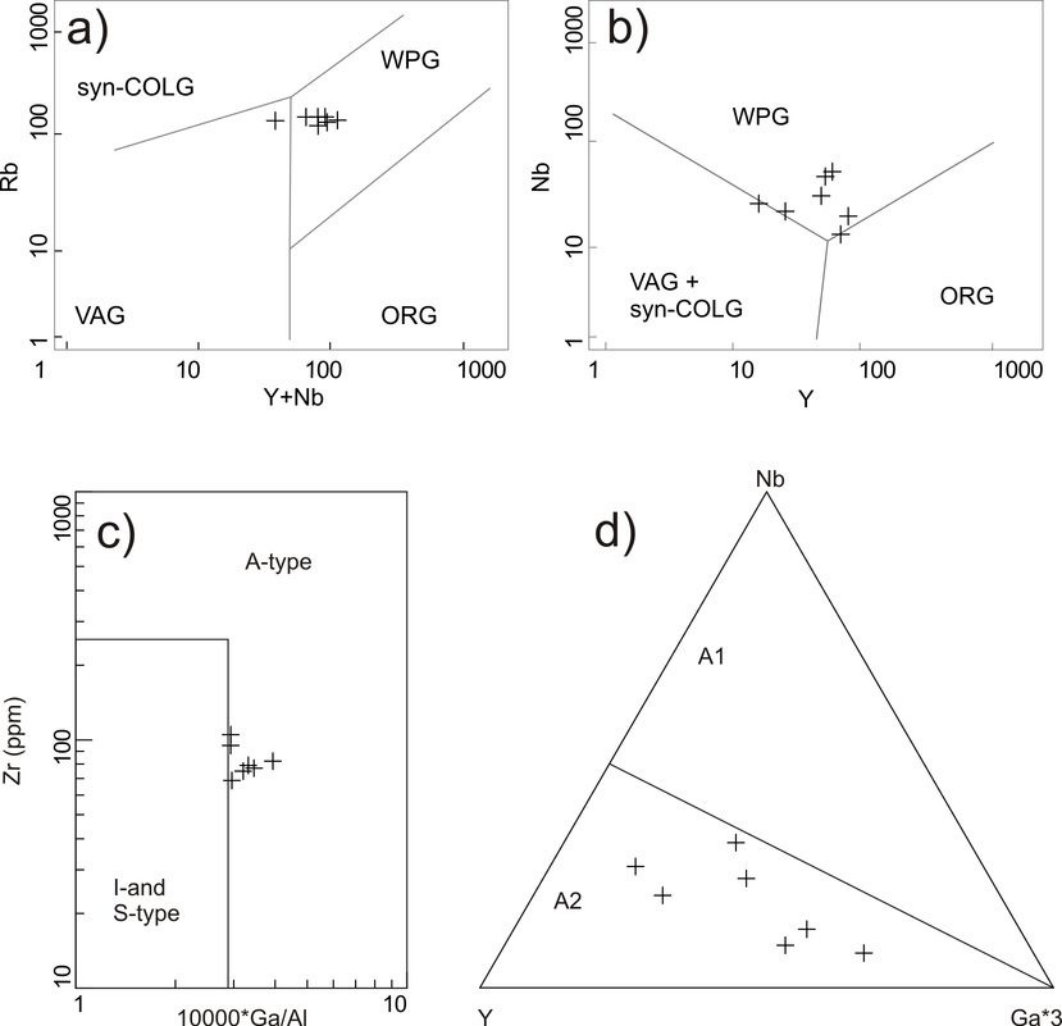
a)
syn-COLG
WPG
VAG
ORG
Rb
Y+Nb
1000
100
10
1
1
10
100
1000
b)
WPG
VAG +
syn-COLG
ORG
Nb
Y
c)
A-type
I-and
S-type
Zr (ppm)
10000*Ga/Al
d)
Nb
A1
A2
Y
Ga*3

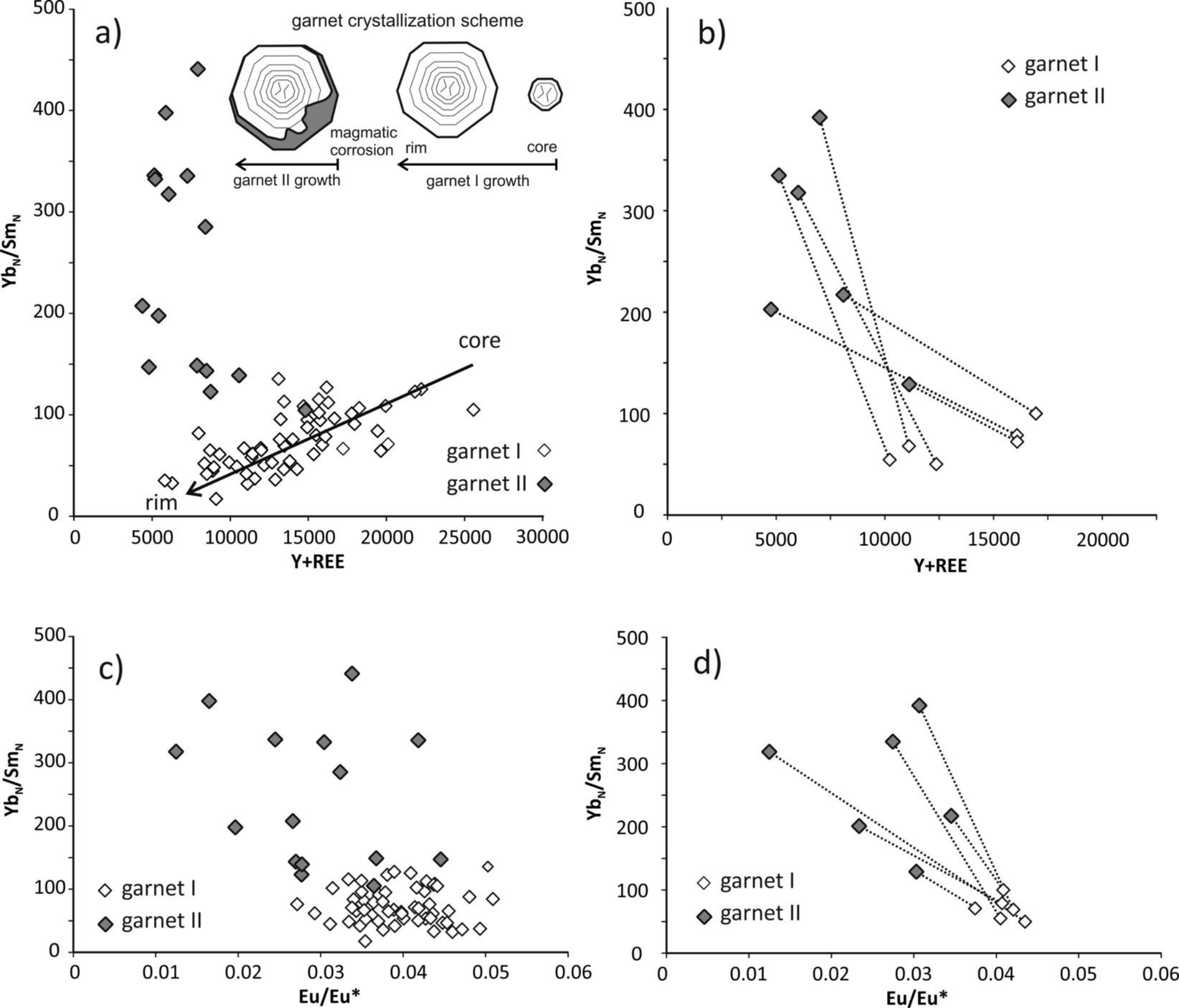
a)
garnet crystallization scheme
magmatic corrosion
rim
core
garnet II growth
garnet I growth
core
rim
garnet I
garnet II
Yb$_N$/Sm$_N$
Y+REE
b)
garnet I
garnet II
Yb$_N$/Sm$_N$
Y+REE
c)
garnet I
garnet II
Yb$_N$/Sm$_N$
Eu/Eu*
d)
garnet I
garnet II
Yb$_N$/Sm$_N$
Eu/Eu*

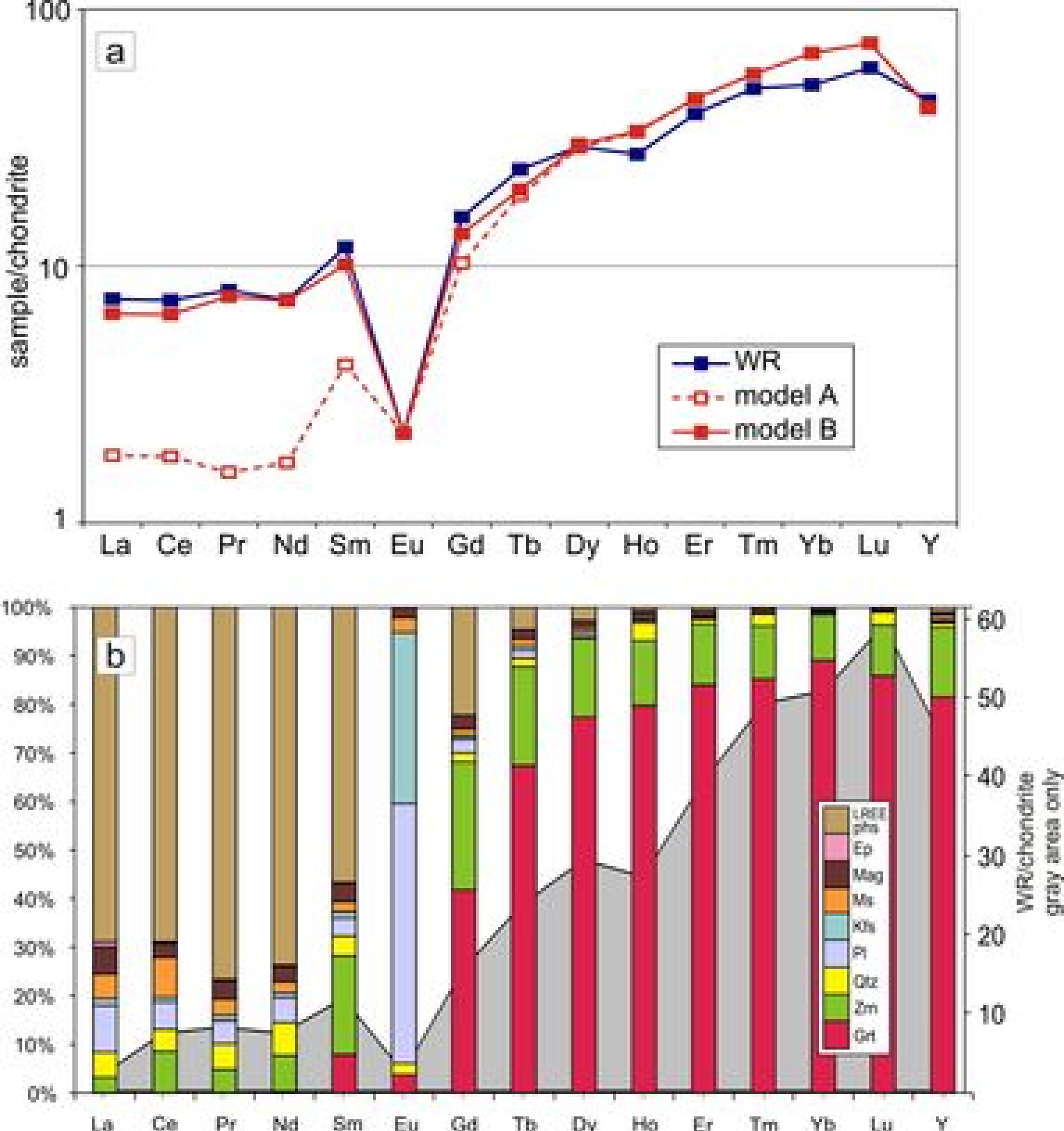
a
100
10
1
sample/chondrite
WR
model A
model B
La Ce Pr Nd Sm Eu Gd Tb Dy Ho Er Tm Yb Lu Y
b
100%
90%
80%
70%
60%
50%
40%
30%
20%
10%
0%
60
50
40
30
20
10
WR/chondrite
gray area only
LREE phs
Ep
Mag
Ms
Kfs
Pl
Qtz
Zrn
Grt
La Ce Pr Nd Sm Eu Gd Tb Dy Ho Er Tm Yb Lu Y

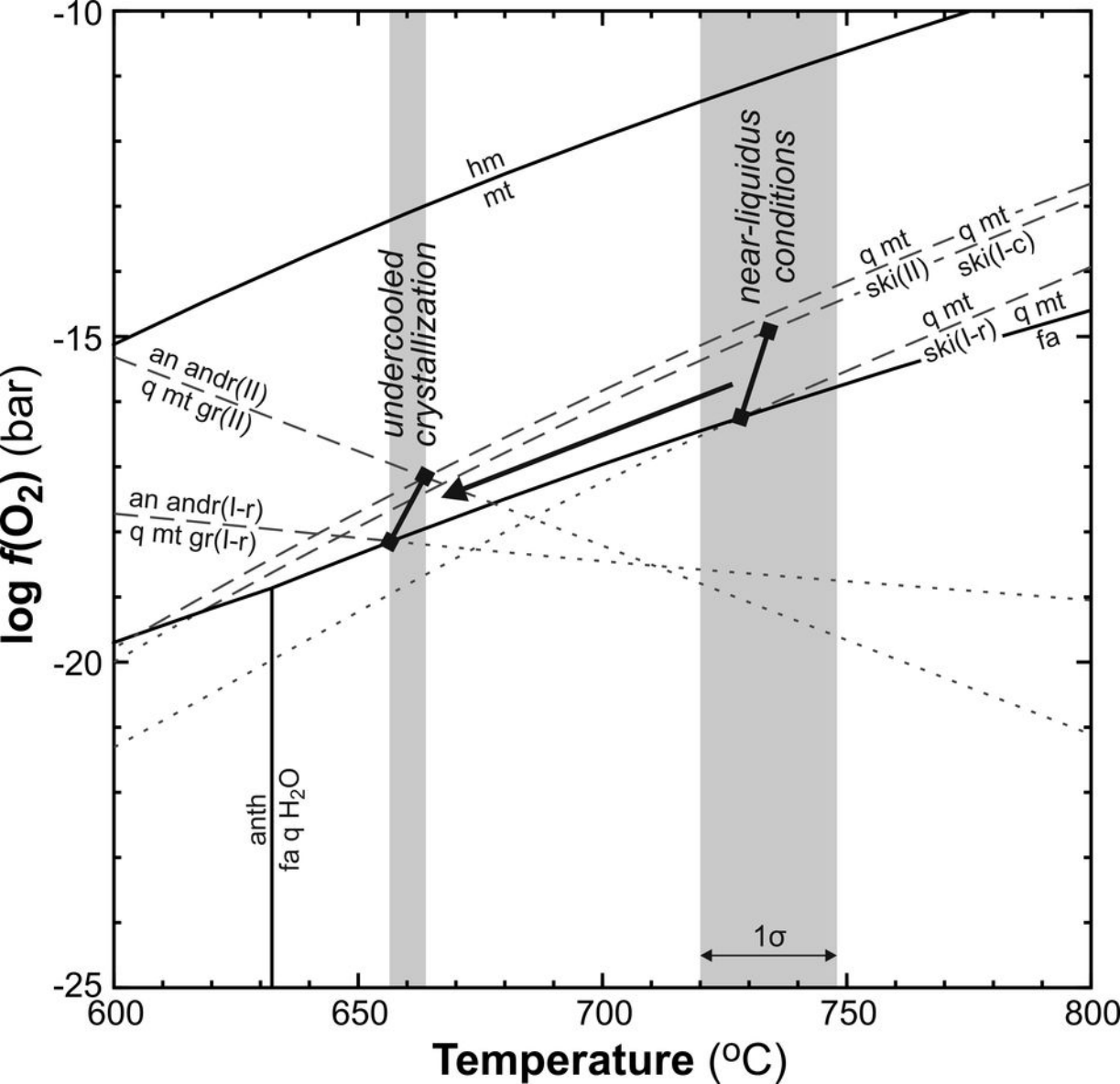
-10
-15
-20
-25
600
650
700
750
800
log $f(O_2)$ (bar)
Temperature (°C)
hm
mt
undercooled crystallization
near-liquidus conditions
q mt
ski(II)
q mt
ski(I-c)
q mt
ski(I-r)
q mt
fa
an andr(II)
q mt gr(II)
an andr(I-r)
q mt gr(I-r)
anth
fa q H_2O
1σ

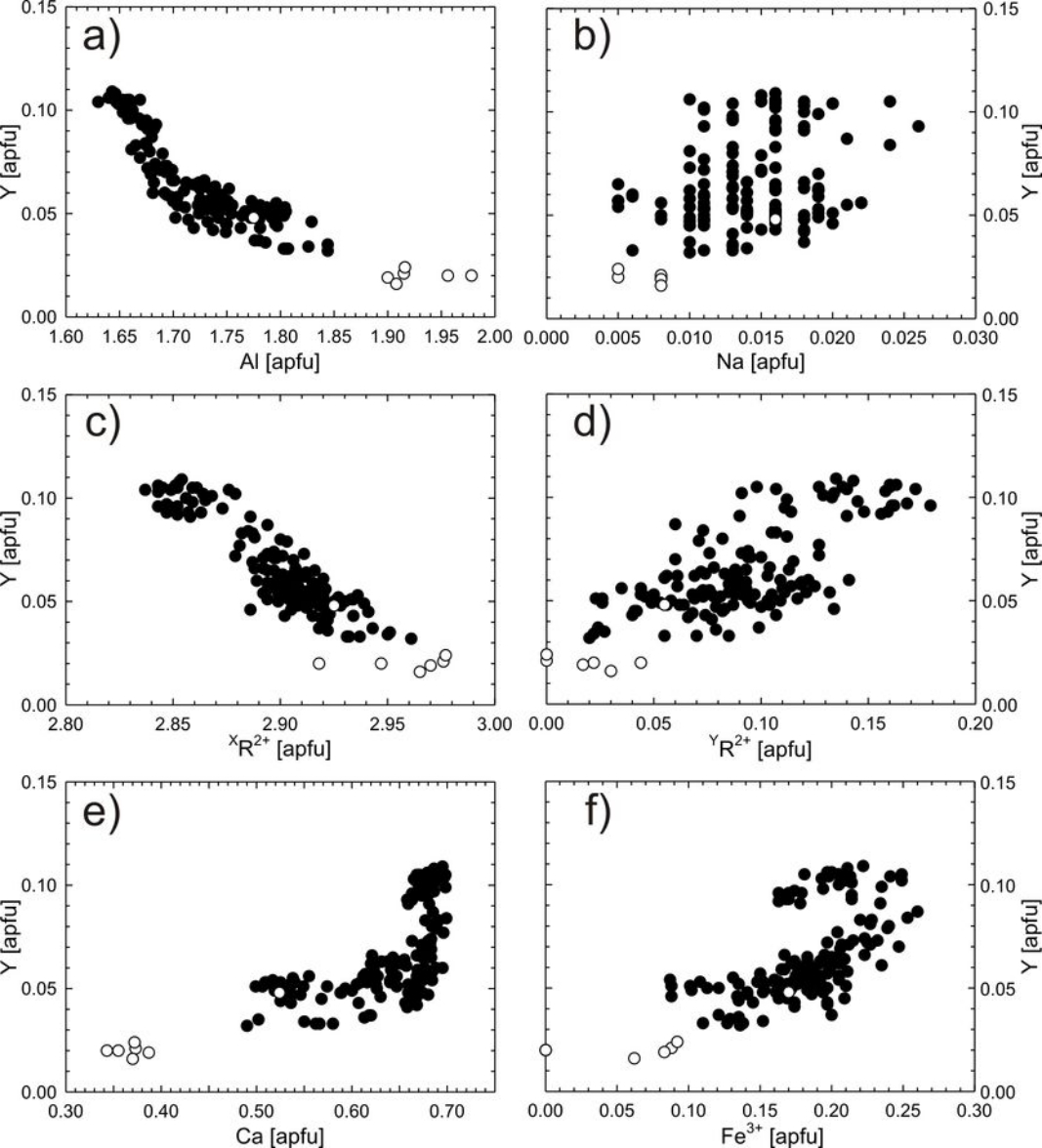
a)
b)
c)
d)
e)
f)
Y [apfu]
Al [apfu]
Na [apfu]
$^{X}R^{2+}$ [apfu]
$^{Y}R^{2+}$ [apfu]
Ca [apfu]
Fe^{3+} [apfu]